Boosting Self-Assembly Diversity in the Solid-State by Chiral/non-Chiral ZnII-Porphyrin Crystallization

By

Wenjie Qian[a], Arántzazu González-Campo[a], Ana Pérez-Rodríguez[a], Sabina Rodríguez-Hermida[b], Inhaz Imaz[b], Klaus Wurst[c], Daniel Maspoch[b,d], Eliseo Ruiz[e], Carmen Ocal[a], Esther Barrena[a], David B. Amabilino[f]* and Núria Aliaga-Alcalde[a,d]*

[a]   Institut de Ciència de Materials de Barcelona (ICMAB–CSIC), Campus Universitari, 08193 Bellaterra, Spain. E-mail:nuria.aliaga@icrea.cat

[b]   Catalan Institute of Nanoscience and Nanotechnology (ICN2), CSIC and The Barcelona Institute of Science and Technology, Campus UAB, Bellaterra, 08193 Barcelona, Spain

[c]   Institut für Allgemeine Anorganische und Theoretische Chemie, Universität Innsbruck, A-6020, Innrain 52a, Austria

[d]   ICREA (Institució Catalana de Recerca i Estudis Avançats), Passeig Lluís Companys 23, 08010 Barcelona, Spain.

 [e]   Departament de Química Inorgànica i Orgànica, Universitat de Barcelona, Barcelona 08007, Spain. Institut de Química Teórica i Computacional de la Universitat de Barcelona (IQTCUB), Barcelona 08007, Spain.

[f]   School of Chemistry, The University of Nottingham, University Park, Nottingham, NG7 2RD, UK.

Abstract: This work bases on the solid-state study of a chiral Zn^{II}-porphyrin derivative (5,10,15,20-tetra[(4-*R,R,R,R*)-methyl-2-phenoxy-propanoate, **1**) building block and its achiral analogous (**2**). Here, foreseen the rich molecular recognition of the designed metallo-porphyrins (**1** and **2**) and tendency to crystallize, we recrystallized both using two sets of solvents (CH_2Cl_2/CH_3OH and CH_2Cl_2/hexane). As a result, four different crystalline arrangements (**1a**-**b**, **2a**-**b**, from 0D to 2D) were successfully achieved. We performed solid state studies for all the species, analysing the role played by chirality, solvent mixtures and surfaces (mica and HOPG), on the supramolecular arrangements. As for the combination of solvents and substrates we obtained a variety of micro-sized species, from vesicles to flower-shaped arrays, including geometrical microcrystals. Overall, our results emphasize the environmental susceptibility of metallo-porphyrins and how this feature must be taken into account in their design.

Introduction

Structural diversity and advanced activity based on supramolecular self-assembly macrocycles are challenging research topics in the field of materials science.[1-2] In the design of non-covalent intermolecular interactions that resembles nature,[3-5] the synthetic methodologies existing are mostly limited by the difficulties of anticipating the final arrangements and the lack of reversibility, where the thermodynamic products are the ending tract, hampering both, control and functioning. Owing to the premature stage of the subject basic studies are required, where a key-point is the use of molecular units that can be easily tailored.

Regarding this, porphyrin derivatives are excellent molecular prototypes due to the possibility of direct information transfer from bench-experiments into biological facts.[6] We can ensure self-assembly because of the sum of its manifold features: (i) the conjugated core that has given copious studies with plenty of data regarding the formation of H/J aggregates;[7] (ii) the use of a metal centre that provides additional interactive site in the final metallo-porphyrins;[8] and (iii) the addition of organic groups in the *meso-* positions of the tetrapyrrolic units that afford extra interactions depending on their number and nature. [1, 9]

Self-assembled aggregates of *meso*-substituted metallo-porphyrins are therefore quite difficult to analyse and specially to anticipate. An approach, adopted by us[10-11] and others[12-13] relies on chirality as the driving force in the achievement of highly ordered structures and the analyses in solution of their noncovalent interactions (hydrogen bonds, π-π stacking or coordination of through the metal centre) and self-assembly mechanisms. However, much less it is known about the genuine effect of chirality on the final architectures, with no strict comparison of chiral/non-chiral analogous porphyrin types, as well as there is scare information on the projection of the knowledge gathered in solution to the solid state. Here, we unify these two ideas toward the analysis of two novel Zn-porphyrins containing phenoxy propanoate and methyl 2-phenoxy acetate groups (**1** and **2**, respectively) in the four *meso-* positions of porphyrins (Scheme 1). The choice of such final entities relates to previous experiences with related systems[10, 14-17] foreseen their rich molecular recognition capacity and tendency to crystallize.

Restricting our recrystallization methods, identical otherwise, for our chiral and non-chiral Zn-porphyrin systems allow new findings in the solid state primarily by the use of X-ray diffraction. In addition, our study integrates the effect of solvent polarity and highlights the polyvalent coordination of the Zn^{II} ions together with the application of solid-state techniques to describe in a great manner the final self-assembled architectures.
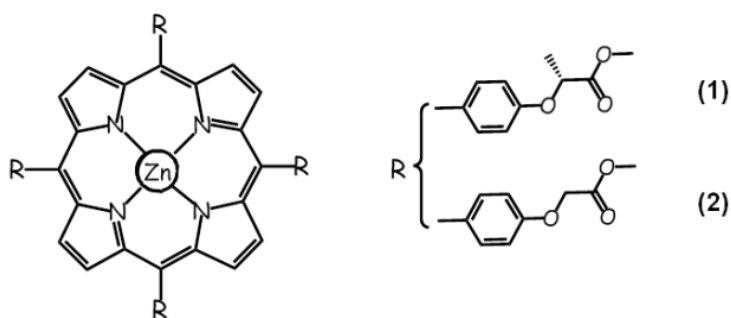
Scheme 1. General scheme of the disposition of the arms in the *meso*-porphyrins, chiral (**1**) and non-chiral versions (**2**).

Here, we do not focus on the dynamics of the supramolecular arrangements but on the outcomes, portraying how small changes can make a great difference in the organization of the porphyrin entities.

Results and Discussion

Metallo-porphyrins recrystallization method. The free porphyrins 4*R*-H$_2$PPP and H$_2$PPP (Scheme S1 top) were reacted with Zn^{II} salts and the resulting coordination compounds (Zn(4*R*-PPP), **1**, and Zn(PPP), **2**) were re-crystallized by slow liquid-liquid diffusion method using CH$_2$Cl$_2$/CH$_3$OH and CH$_2$Cl$_2$/hexane mixtures, respectively (Scheme S1 bottom), when in a final step the samples were left open to air and most of the solvent evaporated. As a result, we found out crystals for all the combinations. **1a** and **2a** for the former and **1b** and **2b** for the second, respectively. Attempts to re-crystallize

the free porphyrins (4R-H$_2$PPP and H$_2$PPP) using the procedure described above did not provide crystals limiting their study to the characterization of **1a**-**b** and **2a**-**b**. (Figures S1-S2)

It has been postulated that solvent mixtures containing water rich solvents can guide self-aggregation processes.[18-19] However, here additional factors require our attention as (i) the non-innocent action of the side groups of the porphyrin cores (noncovalent coordination), (ii) their chiral and non-chiral nature, and (iii) the different coordination possibilities of the Zn^{II} ions; altogether they trigger the final structures (**1a**-**b**, **2a**-**b**).

Structural Descriptions. Table S1 and Figure S3 show general crystal data information of the four Zn^{II}-porphyrin species (**1a**-**b**, **2a**-**b**). Selected bond lengths and angles for each system are listed in Tables S2-S5, respectively, as well as additional Figures in S4-S7 displaying different projections. Overall, the core, for all the porphyrin units shown in **1a**-**b** and **2a**-**b** is identical, described as a Zn^{II} ion coordinated to the N atoms of a porphyrin ring. On the other hand, the main difference between single molecules resides in the chiral centre on the peripheral groups in the formers, as Scheme 1 shows. Here we focus on the major differences between the four species and provide basic molecular descriptions but concentrate in the supramolecular arrangements of all the systems.

[Zn(OH$_2$)(4R-PPP)]. **1a** crystallizes in the orthorhombic $P2_12_12_1$ space group. The mononuclear species contain one penta-coordinated Zn^{II} centre bonded to four N atoms from the porphyrin core and one O from a H$_2$O molecule (Figure 1). The Zn^{II} site is above the porphyrin plane (by 0.207 Å) toward the axially bonded H$_2$O. Such binding is nearly perpendicular to the plane of the Zn-porphyrin core (O-Zn-N angles between 89.85 – 101.43°) with a Zn-O bond length of 2.247 Å. This *meso*-Zn^{II}-porphyrin displays four identical substituents containing chiral ester groups (C45, C49, C53, C57 in Figure 1), all of them with an absolute R configuration. These peripheral moieties, from the 4R-PPP^{2-} system, spread in different orientations from the porphyrin plane with a variety of dihedral angles (-122.04, -109.56, 77.88 and-62.42°).

The supramolecular arrangement of **1a** molecules consists on linear arrays of the porphyrin species, held together by O-H···O hydrogen bonds (Figure 1 bottom, O···O 2.901 Å) between the O from the H$_2$O molecule coordinated to the Zn^{II} centre and the O from the C=O of one of the peripheral arms of a neighbouring porphyrin unit. Thus, every porphyrin is hydrogen bonded to one adjacent moiety. 1D

5

arrays are formed by the linear coordination of one of the four branches of a porphyrin with the nearest neighbour. The Zn-porphyrin molecules in the chain are facing opposite to each other in an alternating fashion, where the hydrogen bonding makes the porphyrin moieties displaced. The chains are aligned with closes distances superiors to 3.3 Å. Further interactions of **1a** molecules between chains lead to the 2D and 3D organizations shown in the SI (Figures S8-S9); in particular, the lattice parameters of the 3D orthorhombic unit cell being a = 9.579Å, b = 17.304 Å and c = 32.657 Å.
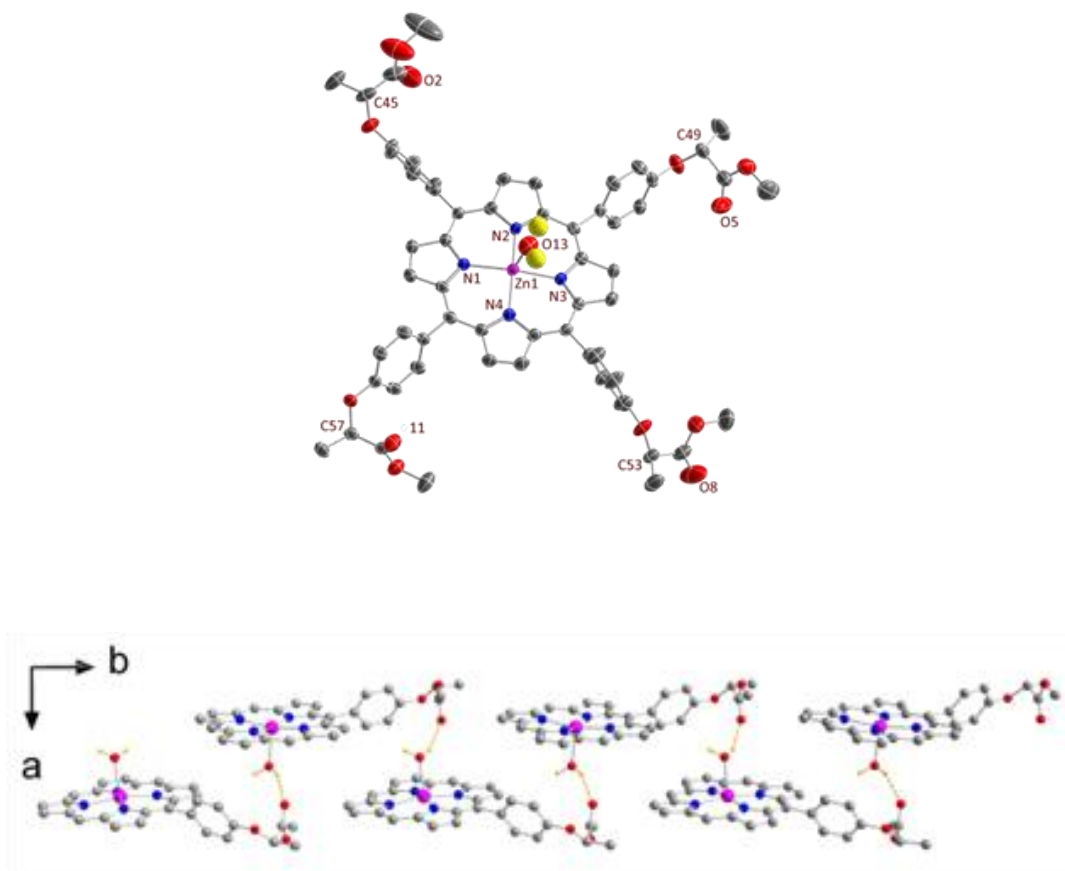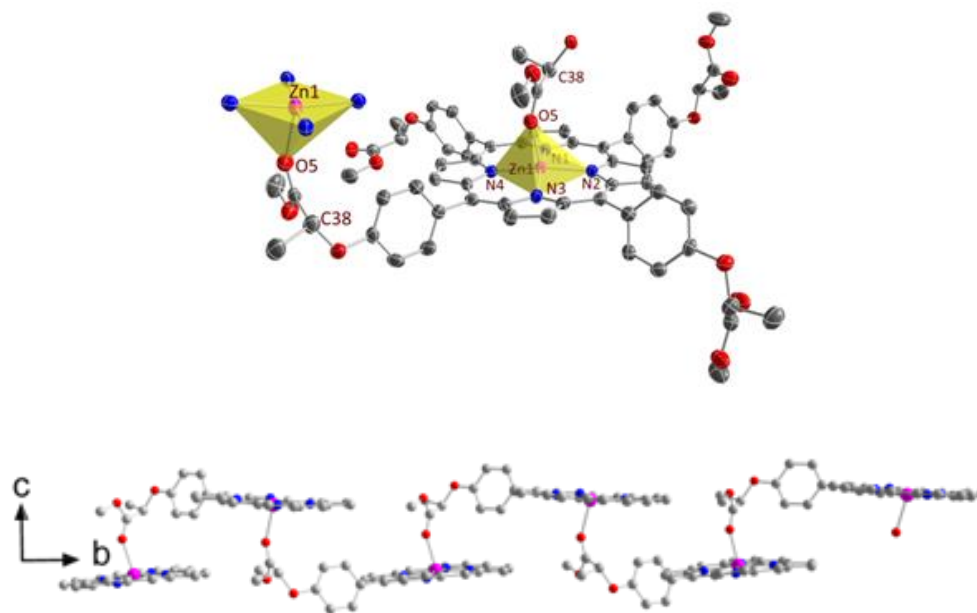

Figure 1. (Top) View of **1a** with thermal ellipsoids fixed at 50 %. Protons are omitted for the sake of simplification. (Bottom) View of the supramolecular arrangement of molecules of **1a**, hydrogen bonding between coordinated H_2O molecules and one specific branch of the porphyrin moieties from neighbour molecules. Hydrogen bonds (except for the ones of the H_2O molecule) and side branches not involved in the intermolecular interactions are omitted for clarity. Color legend: Zn in purple, O in red, N in blue, C in gray, and H in yellow.

The large size of the crystals obtained for **1a** (see inset in Figure 2 and Figure S3) permitted positioning them in the stage of an AFM equipment (see physical measurements) to check the quality of the crystal surface. The surface of this particular 3D crystal as measured by AFM is shown in Figure 2a. It consists of large and atomically flat terraces (several micrometers long and hundreds of nm wide in average) separated by well-defined steps. As it can be extracted from the line profile in Figure 2b, the steps heights are ≈ 1.8 nm, which fully agrees with the crystallographic parameter b and multiples of it (see details of the 3D structure of **1a** in Table S1 in the SI).
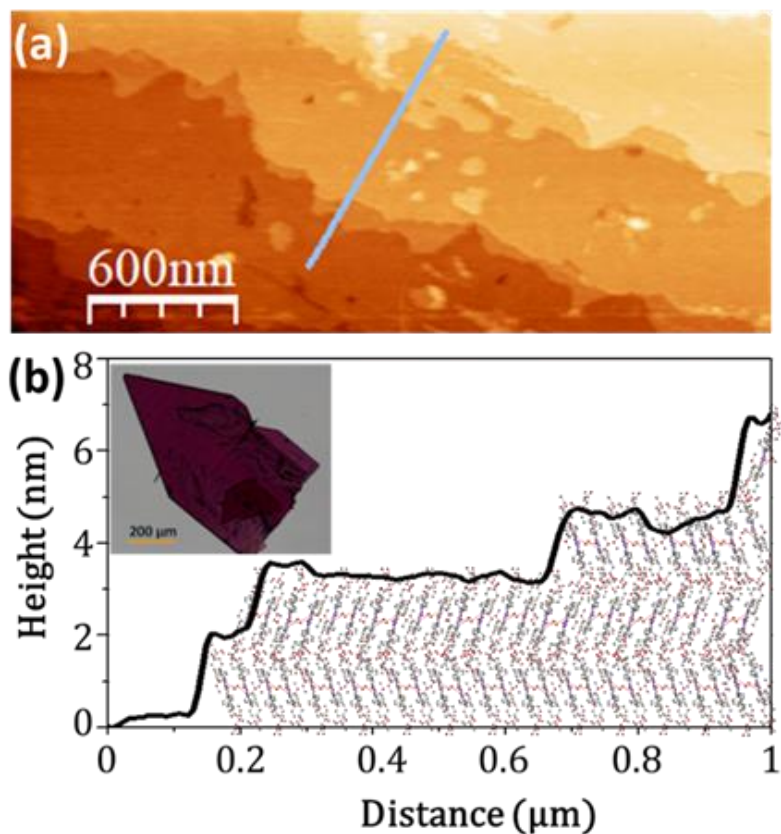
Figure 2. (a) Topographic AFM image of the surface of the crystal of **1a**. (b) Line profile corresponding to the segment signalled in (a). A cartoon with molecules at scale and with the appropriate orientation has been included. Inset: optical image of the particular crystal analysed. Note the sharp angles defining the macroscopic shape of the crystal.

[Zn(4R-PPP)$_n$]. **1b** crystallizes in the orthorhombic *P2$_1$2$_1$2$_1$* space group. **1b** is a coordination polymer made by the self-assembly of the same porphyrin molecule described in **1a** (same porphyrinic ring and chiral branches, Figure 1). The difference now resides in the fact that the Zn^{II} centre of each porphyrin unit is not coordinated to a molecule of H_2O but to the C=O group of an ester branch from the adjacent molecule. Such coordinative bond provides the final polymeric structure depicted in Figure 3. Therefore, each monomeric unit shows a penta-coordinated Zn^{II} centre, with the metal slightly shifted up from the plane of the porphyrinic core (by 0.188 Å). Here, the organic moiety, 4R-PPP^{2-}, presents sprains, where one of the phenyl rings is bended up with respect to the others. The Zn-O bond length distance is now of 2.210 Å, shorter than the Zn-O distance shown in **1a** (Zn-OH$_2$), with a noticeable deviation from previous perpendicular disposition (O-Zn-N angles of 88.60 °, 88.72 ° and reciprocal). As it happened in **1a**, only one C=O from a chiral ester group interacts with the neighbour molecule, leaving free the other three. The final arrangement of a single 1D coordination system is shown in Figures 3 bottom and 4.

Figure 3. (Top) View of **1b** with thermal ellipsoids fixed at 50 %. Hydrogen atoms are omitted for clarity. Color legend as the previous. (Bottom) Arrangement of the coordination polymer (1D system). Side branches not involved in the intermolecular interactions and hydrogen atoms are omitted for clarity.

From our best knowledge, system **1b** is the first chiral coordination polymer of porphyrin nature that is formed by the coordination of one branch of the porphyrin system and one metal of the nearby molecule and the first one displaying chiral properties. Other two coordination polymers have been described in the literature where the metallo-porphyrin units are connected by means of coordinative bounding of the metallic centre and groups from the neighbours, providing also 1D systems.[20-21] However, the ones described in the past, present always the coordination of two branches of the same monomeric porphyrin unit with two others.[22-23]
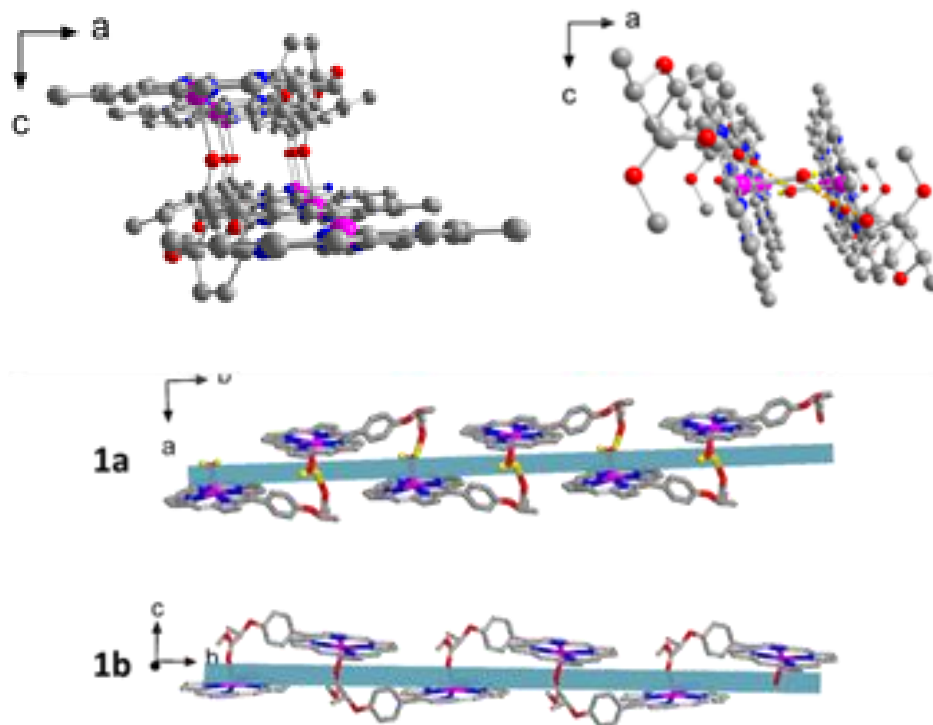

Figure 4. (Top) Side-view of the 1D supramolecular structure of **1a** (left) and the polymeric **1b** system (right) emphasizing the distances among porphyrin units. Side branches not involved in the intermolecular interactions and hydrogen atoms are omitted for clarity. Figures enlarged in SI. (Bottom) Scheme of **1a** and **1b** emphasizing the general orientation of the interactions.

[Zn(PPP)]. Compound **2a** crystallizes in the *C2/c* monoclinic space group and the discrete unit consists exclusively in one molecule of the Zn^{II}-porphyrin moiety. Here, the Zn^{II} centre is tetra-coordinated and adopts a square planar geometry, forming a perfect plane with the four porphyrin nitrogen atoms of

9

the core. The planarity of the PPP^{2-} ligand does not present any deformation, in contrast with what it happens in the units of **1b**.

As Figure 5 (Top) shows, the structure has some resemblance to that describe in **1a**, due to the similarities of the peripheral groups, but now the replacement of the CH$_3$ group in all four branches by a proton lets to achiral molecules. Although the compacted packing of the molecules shows proximity among neighbours, the Zn^{II} centre in **2a** is further away from the C=O moiety (3.333 and 3.908 Å) and no molecules of solvent/H$_2$O appear in the final supramolecular architecture (Figure 5, Bottom).
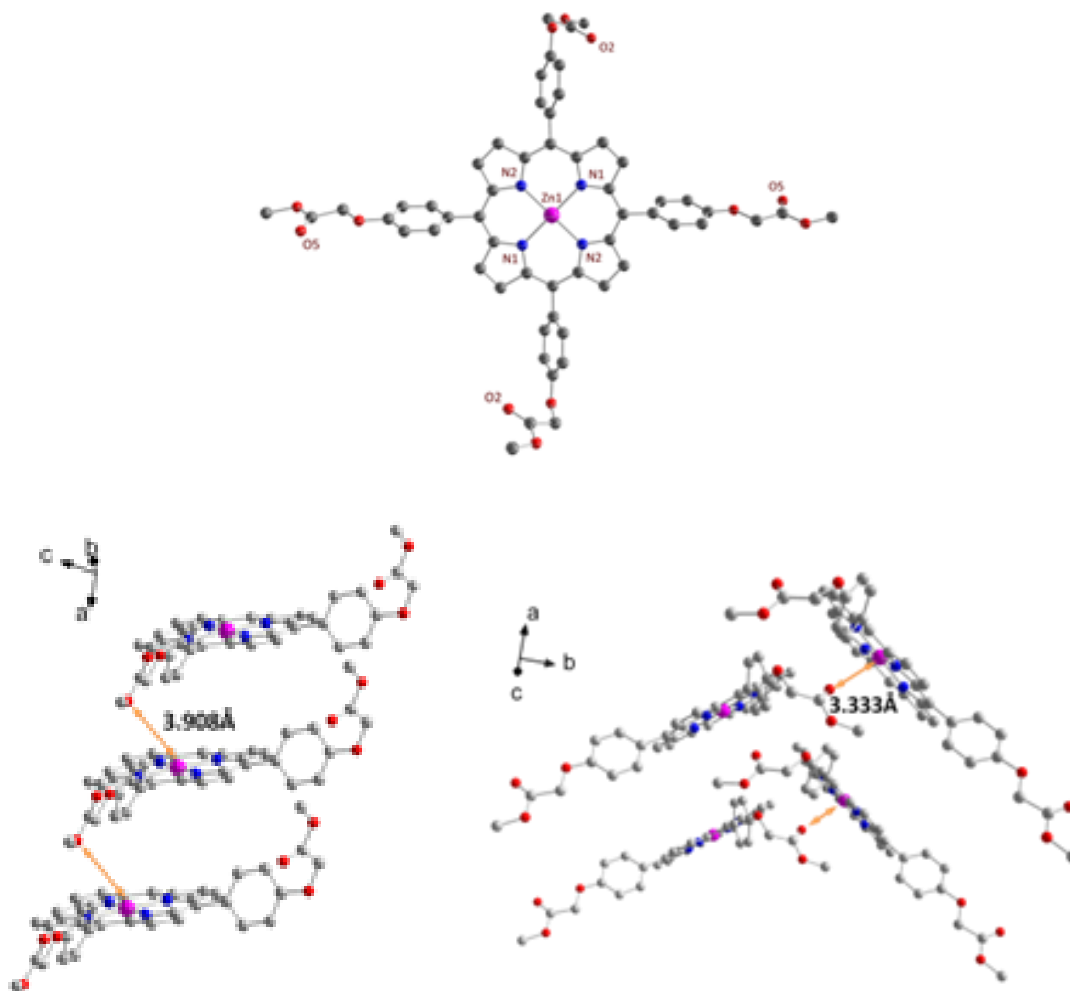
Figure 5. (Top) View of **2a** with thermal ellipsoids fixed at 50 %. Hydrogen atoms are omitted for clarity. Color legend: Zn in purple, O in red, N in blue and C in gray. (Bottom) Side views of the disposition of **2a** molecules and intermolecular interactions among them. Some of the side branches not involved in the intermolecular interactions and hydrogen atoms are omitted for clarity.

[Zn(PPP)$_n$]. **2b** crystallizes, as the previous, in the monoclinic space group *C2/c*. The asymmetric unit is described by a molecule of "Zn(PPP)O$_2$", where the oxygen atoms relate to the C=O groups of two neighbouring molecules (Figure 6, top). The Zn^{II} centre is therefore hexa-coordinated, with a pseudo-octahedral symmetry due to its coordination to four nitrogen atoms from the PPP^{2-} organic moiety and to the two oxygen atoms already mentioned. As it happens in **2a**, the Zn^{II} centre forms a perfect plane within the chromophore core. In the rearrangement, the oxygen atoms are tilted from 90° (84.27°, 85.64° and reciprocal). Each ZnPPP is attached to four other units creating 2D networks with *sql* topology, where the Zn^{II}-porphyrin molecules present alternating orientations and one single Zn···Zn distance of 13.663 Å (Figure 6, bottom). The structure grows layer by layer, where the adjacent 2D networks are parallel to each other with small interactions between them through the branches that are not involved in coordination (Figure S10).
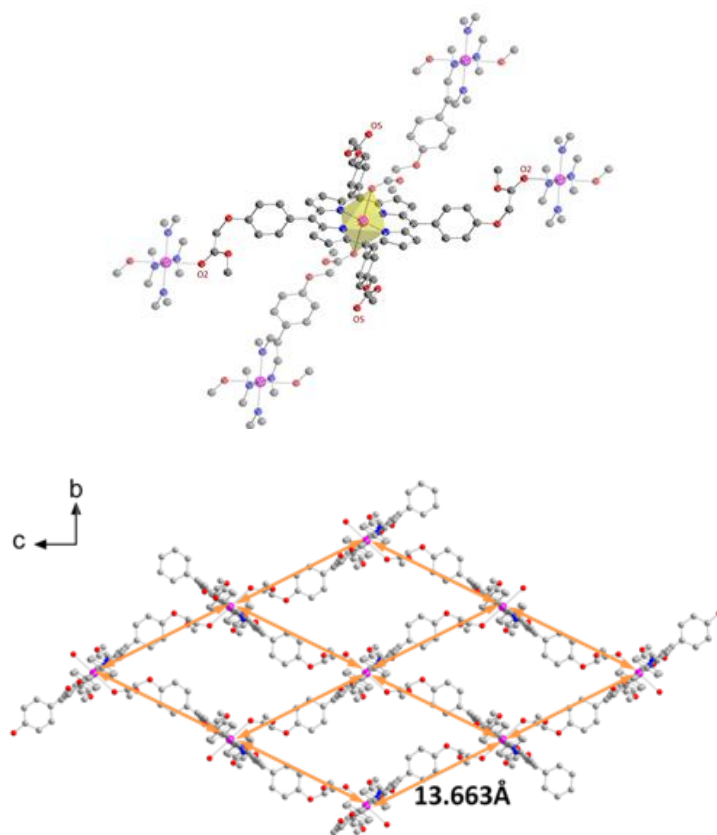
Figure 6. (Top) View of **2b** with thermal ellipsoids fixed at 50 %. Hydrogen atoms are omitted for clarity. Color legend: Color legend: Zn in purple, O in red, N in blue and C in gray. (Bottom) General view of nine molecules of **2b** forming the 2D structure. Zn^{II}···Zn^{II} distances are in all cases 13.663 Å.

Altogether, we found two Zn-porphyrin setups (**1** and **2**) with great ability toward crystallization, and confined the combination of solvents for such task (CH_2Cl_2/CH_3OH and CH_2Cl_2/hexane) to investigate chirality and polarity. By doing so, we created a map with a rich variety of supramolecular arrangements.

Having a Zn^{II} centre and four terminal benzylic ester moieties at the *meso-* positions, both electron-acceptor and donor parts in that order, we expected self-assemble through coordinative bonds, fact that we see in two of the systems under study, **1b** and **2b**. However, the final picture is more complex, where the coordination number of the Zn^{II} metal centre varies from four to six, unlikely to anticipate. Single crystal X-ray diffraction shows that in the case of the chiral systems, **1a** and **1b**, the Zn is always pentacoordinated, choosing as the fifth ligand a molecule of H_2O or the terminal benzylic branch of one neighbouring species, respectively. The same methodology applied to the non-chiral versions provides tetra- and hexacoordinated Zn^{II} centres, **2a** and **2b**, respectively. In all cases, the size and geometry of the crystals for all the four samples differ (Figure S10). We could argue that the changes in solubility regarding the existence of a $-CH_3$ vs. a $-H$ (**1** vs. **2**) in the winds of the porphyrins, makes unfeasible a rigorous comparison but the two methodologies used work in a similar manner in the four systems, having crystals in all the cases after few days. Therefore, chirality may be involved in the results; where the $-CH_3$ of the coordinated branches are always outside, improving the disposition of the C=O group toward the Zn^{II} centres (Figure S11). Here, it is worth mentioning the formation of (supramolecular or covalent) 1D structures, that display helical shapes along the direction of the chains (Figure 4 bottom), only in the case of the chiral systems (**1a** and **1b**). This is a key factor for the finding of chiral response in the solid state for such species, absent in their achiral versions.

On the other hand, the polarity of the solvent provided us with additional features, where the use of CH_3OH as a precipitating agent gave always isolated molecules (0D). Here, the intermolecular associations within discrete porphyrin coordination compounds rely on H-bonds involving coordinated water molecules (**1a**), or C-H···π interactions (**2a**). Instead, hexane always provided compact supramolecular moiety, although compounds **1b** and **2b** present different arrangements. This seems to indicate that the most apolar solvent forces aggregation of the molecules that re-organize through the metallic cen-

tre and moieties on the arms. The differences in the self-assemble however, must be related to the affinity among the molecules and therefore to the nature of such branches, chiral and achiral.

In addition, studies in solution by ^{1}H NMR and UV-Vis absorption spectroscopy in CD_2Cl_2 (Figures S12-S14) of all Zn^{II}-porphyrins showed isolated porphyrin units, chiral (Zn^{II} (4R-PPP), **1**) and achiral (Zn^{II}(PPP), **2**), with no additional info regarding aggregation even at different concentrations (Figures S12, S13). In the case of **1**, the absence of CD signals using the same solvent was expected, due to the distance between the chromophore core and the chiral centres and the freedom of rotation of the latest.[24] MALDI experiments of **1a** and **1b** in CH_2Cl_2 provided almost identical spectra, showing one m/z signal with maximum at 1084.29 and isotropic patterns that matched well with the existence of [Zn^{II}(4R-PPP)] units. Additional experiments were performed with samples **1a** and **1b** to contemplate the origin of the coordinated H_2O in the case of **1a**, missed in **1b**. For that, we used dehydrated Zn acetate salts and play with the H_2O content of the solvents following the same methodology explained above. Our analyses showed that the the H_2O molecules from crystal processing, therefore contained in the solvents used to recrystallize the samples (Figure S15).

In a further step to characterize in detail the systems and chiral nature in the case of **1a** and **1b**, we gathered information with the use of current and specialized solid-state techniques, having the advantage of correlating the changes to the structures described above. The following paragraphs describe the outcome encountered and our impressions regarding their practical use.

Solid state studies. In a first step, we performed XRD analyses on different crystalline batches for each compound (**1a**-**b**, **2a**-**b**) for phase identification and consistency of the final structures. Figures S16-S19 depict the diagrams found experimentally for the four species and the comparison with their simulated spectra, respectively. **1a**-**b** and **2a** presented reproducible patterns that allow us to use crystalline samples toward additional characterizations in the bulk shown below. However, crystals of **2b** were scarce. Attempts to recrystallize such solid showed PXRD patterns that differed from the expected from the powder pattern of **2b**; this was a drawback for the rest of the analyses in the solid-state where high amounts of samples were required. Hence, the comparison of **2b** with the rest of systems was limited to the crystallographic information.

13

Following with our analysis, ATR-FTIR provides us clear evidences of the changes shown in the crystal structures. In the case of the chiral systems, **1a** and **1b**, the two molecules present almost identical ATR-FTIR spectra but differing in two areas between 3450-3470 cm^{-1} and 1720-1760 cm^{-1} (Figures S20). The former area shows the appearance of a broad peak in the case of **1a** missing in **1b** that may correspond to the inserted H_2O molecule as the structure shows. On the other hand, the former area relates to the C=O stretching vibrational modes from the terminal ester groups of the four branches. In the case of **1a**, appear two peaks at 1732 and 1750 cm^{-1} but **1b** shows three peaks, at 1719, 1739 and 1757 cm^{-1}, agreeing well with the fact of having one ester group coordinated, different from the rest. Regarding the same area, compound **2a** displays a single peak with a shoulder at 1752 cm^{-1} (Figure S21) and in agreement with the absence of different coordination on the branches with Zn^{II} centres. Thermogravimetric analyses (TG-DSC) of **1a**-**b** and **2a** were also carried out. **2a** and **1b** show critical weight loss above 200 °C and 300 °C, respectively; TG data of **1a** displayed the release of water molecules starting at 85 °C (Figure S22).

Our studies show that the existence of different supramolecular formations has scarce effect on the solid-state UV-Vis absorbance of the final systems, remaining all, chiral and achiral, very similar as it happens in solution (Figure S23). Additional fluorescent experiments in solution or solid state were not further pursued.

On the other hand, high-resolution solid-state ^{13}C NMR spectroscopy was one of the most sensitive techniques for our studies; Figure 7 shows the spectra of **1a**, **1b** and **2a** (4R-H$_2$PPP is shown in Figure S24). The general assignments of the chemical shifts were made by comparison with the free achiral porphyrin and the contrast among the coordination compounds (**1a**-**b** and **2a**) and reported literature.[25] From the latest, similarities of our porphyrins to the 5,10,15,20-tetraphenyl porphyrin Zn^{II} compound, studied by Grant *et al.*[26] allowed us to interpret the nature of most of the chemical shifts by their range of appearance although specifics about individual shift assignations were not possible to elucidate.
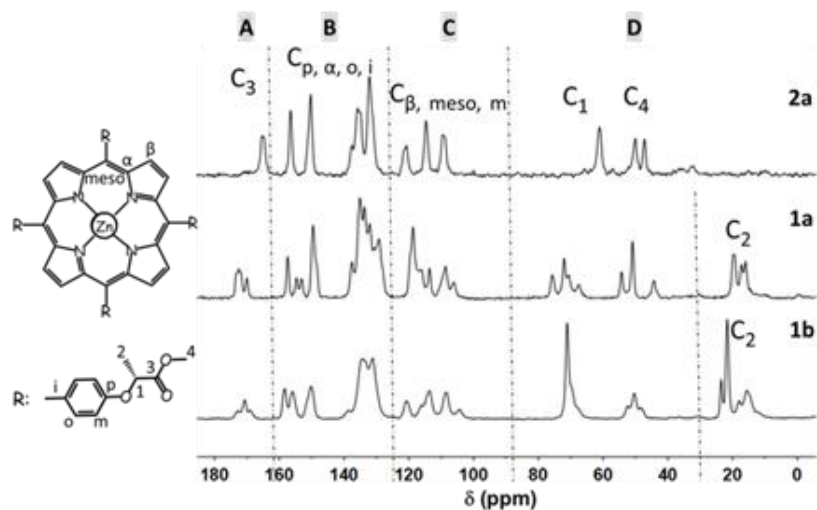
Figure 7. Comparison between the solid-state ^{13}C NMR spectra of **1a** (top), **1b** (central) and **2a** (bottom) between 180 – 0 ppm.

We found out that multiple signals appeared in the range of 180 to 0 ppm for compounds **1a** and **1b** and from 180 to 30 ppm for **2a**. The shifts could be grouped in four areas: signals appearing between 180-165 ppm (A), 165-125 ppm (B), 125-100 ppm (C) and from 80-20/0 (D), from down fields to high ones (Figure 7). "A" encloses C3 (Figure 7), related to the C=O part of the ester. "B" is the sum of C_{para}, C_α, C_{ortho}, C_i and probably part of the C_β shifts. "C" would include C_β, C_{meso} and C_{meta} and finally "D" will rely to the non-conjugated part of the molecule (branches) therefore to C1, C4 and C2, from down to high fields, in that order. The absence of C2 in **2a** (Figure 7) corroborates our assignation in the other two systems (**1a** and **1b**).

The variation in the number and shift of the chemical signals differ, from one sample to another, in a complex manner. It is already established that such variations can relate to overlap of the signals, small structural differences inside the molecules (e.g.: bendings provide different number and shifts for C_β, C_α, etc.) and to the proximity of neighbouring molecules (e.g.: π electron cloud of the core) providing different environments to most of the groups.[27] Comparing **1a** and **1b**, the multiple chemical shift corresponding to C3 of **1b** suffers (at least one over four per molecule) such alterations in a strong manner than the others. The final shape of these signals is different in both and shifted to higher fields

for **1b** (172.5 ppm (**1a**) and 170.7 ppm (**1b**)). The shift and shape of C1 also clearly differs in all three systems showing the dramatic effect that different environment has on the chiral/achiral carbons.

Chirality. Taking advantage of the chiral nature of some of the samples, we performed solid-state circular dichroism studies of **1a** and **1b** using a KBr matrix due to the absence of chiral response in solution. The key aspects for finding optimum conditions in the achievement of the spectra were described elsewhere[28-29] and detailed information regarding our procedure here is described in the SI. In the past, some of us studied the correlation of experimental Cotton effects (CE) with the conformational stereoisomerism of chiral systems in the solid state.[30] Our objective here was to establish the relationship between the CD spectra of the compounds and their supramolecular conformations, comparing systems with identical chiral species. Figure 8 shows the comparison between the two species (**1a-b**) under such conditions and Figure 4 bottom emphasizes the crystallographic disposition of the two compounds. Here again, it is important to underline the spatial disposition observed in both systems (missed in the achiral structures) that give rise to helical architectures in the chains (supramolecular and coordinative 1D arrangements, for **1a** and **1b**, respectively).
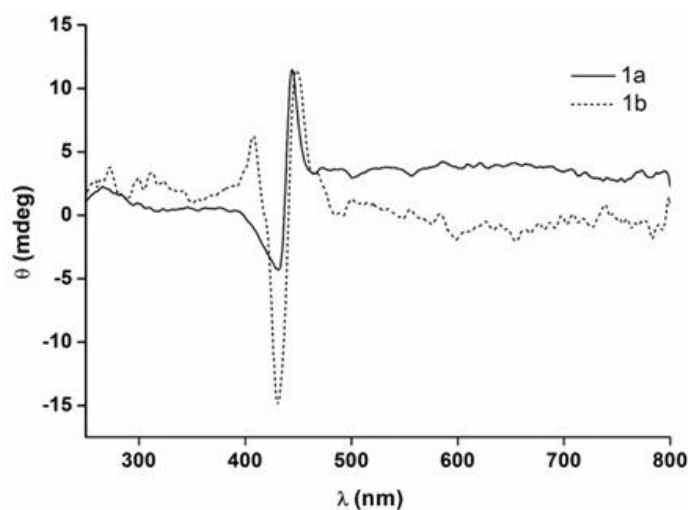
Figure 8. Solid state CD spectra of **1a** and **1b**.

Taking advantage of the collected X-ray diffraction data, we now could match structural differences between the molecules with changes in the CD spectra. This way, the R-nature of the ligand, for **1a**

16

shows a bisignate signal displaying a negative CE at the lowest wavelength and a positive Cotton effect of similar intensity at higher wavelengths. This matches well with the position of the Soret absorption band of the porphyrinic chromophore in solid and solution (Figure S28), where the presence of bisignate CD may also relate to the orientation of the porphyrin cores in a sliding face-to-face creating a 1D supramolecular structure through the H_2O interactions (Figure 1 bottom and 8 bottom).

In the solid state, compound **1a** displays two intense and proximate CD bands of opposite sign (positive-negative; positive chirality)[31] between 375 and 500 nm (black solid line) centred at 431 and 444 nm, respectively. In the case of **1b** (dotted line), CE are observed in the same range, although now three CD signals appear (positive-negative-positive) being the one in the middle the most intense.

The above features are present in the CD spectrum of **1b** too, however, this system differs from the previous by displaying a third positive CD signal, absent in **1a**, headed by the already mentioned strong positive-negative bisignate CD sign. The negative Cotton effect is here more pronounced than for **1a**. Such results could be associated to the expanded 1D coordination network of **1b**, by the coordination of the Zn^{II} centres with CH_3CO_2-*R* moieties (instead of molecules of H_2O (**1a**)) and differences in the tridimensional packing between the two systems (Figure 8 bottom).[32] The first positive CD signals (highest wavelengths) for the two systems, **1a** and **1b**, with maxima at 444 nm and 448 nm, respectively, follow similar trends, and intensity, having again close relation to the Soret band and therefore intrinsic structure of the otherwise identical porphyrinic units. These results highlight the high sensitivity of the technique and how smooth supramolecular arrangements can tune the appearing signals. They also show the advantage of using chiral sources to study changes in self-assembly.

Finally, we analysed the chiral systems using solid-state vibrational circular dichroism (VCD). VCD has great advantages toward the detailed analysis of molecular conformations because the number of molecular vibrations, in the IR region, and the sensitivity of the technique are larger than the electronic transitions in the UV-Vis region.[33]

Nevertheless, working in the solid state one must be extremely careful minimizing the spectral artefacts. For that, we took into account the noise in each experiment, the signals found in the non-chiral system **2a** (Figure S29) and performed theoretical calculations on **1a** (Figure S30). The workout of the material and procedure is described in the SI. Figure 9 shows the comparison between the IR and the

VCD spectra of both systems. As expected, each absorbance band in the IR spectrum has a correspondence with a VCD band. DFT geometry optimization and frequency calculation were performed (all-electron 6-311G* B3LYP[34] calculations using Gaussian09 code, [35] see Fig. S31) taking into account the single molecule **1a** (the length of the chain of **1b** difficult the study) displayed a number of motifs in the window under study in a similar manner although few shifted from the experimental values displaying, at times, opposite sign from the observed. Albeit contradiction, such results point out that the chiral response of the system involves the surroundings, where the supramolecular network is the responsible for the chiral phenomenon.[36]
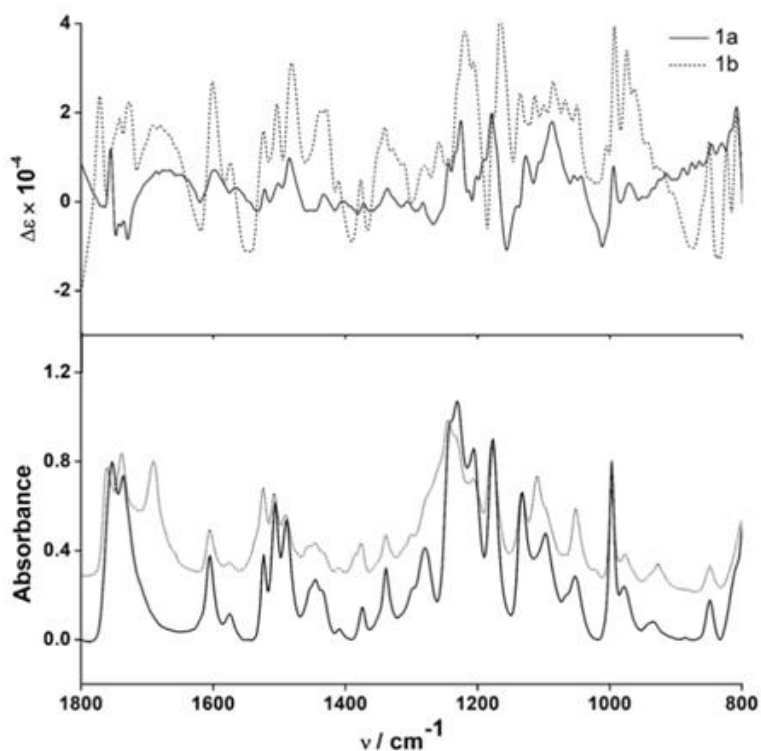
Figure 9. Solid state VCD spectra (top) and solid-state absorbance IR spectra (bottom) of **1a** and **1b**.

The measured and calculated VCD spectra of each system match well with those found in the IR experiment corresponding to 4R-systems (intensities are not comparable). The bands described between 1800-1600 cm^{-1} vary between the two species, as anticipated due to the difference upon coordination of the Zn^{II} centres of the porphyrinic moieties with H_2O (**1a**) or some C=O groups (**1b**). In this region,

18

the number of VCD bands found in this region for **1b** is higher than **1a**, with some of them shifted to lower energies, probably due to the difference between the C=O groups bounded with respect to the non-bounded ones and additional intermolecular interactions in the tridimensional map of each system.

Overall, all the techniques used in the solid-state studies agree with the structures but emphasize their restricted outcome individually.

Surface studies. We performed SEM images of the samples prepared by drop casting solutions (10^{-3} M) of the chiral (Zn(4*R*-PPP), **1**) and achiral (Zn(PPP), **2**) porphyrins in the same solvents mixture used to achieve **1a**-**b** and **2a**-**b**: CH_2Cl_2/CH_3OH (1:1) or CH_2Cl_2/hexane (1:1), respectively, onto mica or highly oriented pyrolytic graphite (HOPG) substrates. Here, the effects of solvents and surfaces were studied by the comparison with the morphologies found in the single crystal X-ray diffraction experiments. A variety of Zn(4*R*-PPP) and Zn(PPP) nanoarchitectures were obtained by an evaporation-driven self-assembly process (Figure 10). The chiral and achiral porphyrins generate reproducible microvesicles, microrods flower-shaped aggregates and microplates bundles shapes, depending on the conditions used (Figures 10a-d and S31-S40).

Hollow microvesicles appeared by dissolving **1** in CH_2Cl_2/CH_3OH and depositing it on mica (Figures S31) and graphite (Figure 10a and S32). On mica, the size and shapes of the aggregates were the most irregular, presenting sometimes sectioned microvesicles; instead, on graphene the microballs presented an average size of 600 nm with hole diameters of ~300 nm. Overall, the vesicles in the latest were distinguishable and presented homogenous shapes, where some of them connected to others through small cords. In CH_2Cl_2/CH_3OH, hollow vesicles made of Zn-porphyrin systems have been related to the ⬜⬜⬜ stacking of the porphyrin rings and formation of J-type aggregations.[37] Guided by the crystallographic data of **1a**, we can relate our porphyrin microvesicles to the ligand-assisted long-distance J-type formation[38] In our case, the supramolecular 1D structure of **1a**, with up-down distributions of the porphyrins cores (Figures 1-bottom and S33), differs from the regular staircase situation described in previous works.[39] The general explanation for the holes formation, of encapsulation of the volatile solvents inside the vesicles and later evaporation, is also applicable here.
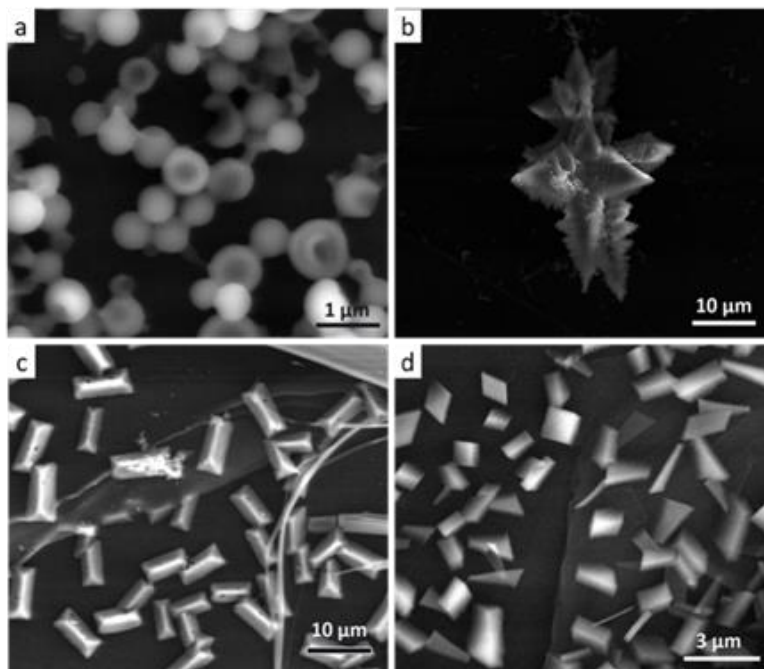
Figure 10. SEM images on HOPG substrates of Zn(4*R*-PPP) prepared in CH$_2$Cl$_2$/CH$_3$OH (a), Zn(PPP) in CH$_2$Cl$_2$/CH$_3$OH (b), Zn(4*R*-PPP) in CH$_2$Cl$_2$/hexane (c) and Zn(PPP) in CH$_2$Cl$_2$/hexane (d).

Repeating the same exact experiment but using **2**, the architectures found on mica and graphene were totally different than before. Now, on mica well-shaped microcrystals of different sizes presented parallelogram and prismatic geometries (Figures S34). On graphite, four-pointed star shapes were the most common morphology (Figures 10b) although bigger and amorphous aggregates were seen too (Figure S35); all shapes intuitively relate to the layer-by-layer aggregation present in the structure of **2a** (Figure 4-bottom) and to the formation of short-distance J-type aggregates (staircase disposition). Overall, the quantity of material deposited on the different substrates limited the use of additional techniques, as for example XRD, toward the possible identification of **1a/2a** or related species. Nevertheless, it is important to stress the differences in morphology between the chiral and achiral units, providing the first microvesicles and the second prismatic shapes. Taking into account that the comparison was performed in an identical manner (hence, mixed of solvents and surfaces), the difference between the two obvious architectures may reside in their intrinsic nature, chiral and achiral.

Moving to CH_2Cl_2/C_6H_{14}, with **1**, on mica, we observed again microballs, some of them with holes, together with slide microvesicles (Figure S36). The difference with the previous resides in that most of the microball edges smear, connecting each other, probably because of solvent flow and the longer sintering state during the evaporation process. The shape of the nanostructures agrees well with **1b**, where the 1D coordination structure provides J-type aggregates (up-down structure, Figure 3-bottom). On graphite, two distinctive morphologies were observed depending on the area of analysis. This way, some of the parts presented microvesicles with sizes between 300-400 nm (Figures S37). The topographic information in such cases was very similar to that found in CH_2Cl_2/CH_3OH; however, trigonal prisms were observed mostly at the surface edges (Figure 10c). They presented homogeneous sizes, with a length of 8 ▯m, and spherical defects in some of the prismatic faces (Figures 10c and S38). Such prismatic microcrystals show similarities with those at the macroscopic scale used for the X-ray diffraction analysis (Figure S3). They were in areas where the evaporation process is slower, providing more time for the ensemble and organization of the matter. This was established by the fact that few of them appeared cracked exposing the aggregation of microvesicles like expanded polystyrene bowls (Figure 10c).

At last, the same mixture using **2** on mica showed microplates, with diverse shapes and sizes, together with flower-shaped topologies (Figure S39). In former works, the formation of the latest relates usually to H_2O.[40] Here this association cannot be discriminated but neither defended. However, in both cases, in microplates and micropetals, it is clear the existence of an extended face versus the others, connecting with the 2D layers observed in the **2b** system typical in other layered materials as well.[41] Regarding the experiment in graphite, now multiple microblocks were present again with a variety of sizes and prismatic shapes (Figure 10d and S40). The size may depend on the deposition and evaporation processes, where the concentration of the material can also rely on the different terraces of the graphite surface. Either way, this result differs with the macroscopic scale in solution, where the crystals were scarce and difficult to achieve, pointing out the tendency of graphite to provide crystalline material under these conditions.

Conclusions

Using metallo-porphyrin derivatives as unit models, we described how through a unique molecular design, we created well-defined and isolable nanostructures; where, the tuning of solvent conditions directly affected the self-assembly process, and therefore the morphologies of aggregates. Our results emphasize the relevance of porphyrin crystallization toward their future applications and face the present challenges, as the lack of anticipation of the final architectures. The addition of a metal centre increases the range of diversity in the coordinative way meanwhile blocks strong ▯▯▯▯stacking interactions among the porphyrin cores giving priority to the nature of the arms, now key parts in the creation of the supramolecular arrays. The four arms are flexible enough and the carbonyl moieties, from the ester groups at the edges, present the freedom to attach the Zn^{II} centres in different manners where the final coordination number of the metallic centre can go from four to six, depending on the overall conditions. The comparison between chiral metallo-porphyrin (**1**) and non-chiral (**2**) one, repeating exact conditions, provides different crystallographic species, pointing out the complexity of adding chirality among the other factors already mentioned (coordination and solubility). The nature of the precipitant solvents, from polar (CH_3OH) to apolar (C_6H_{14}), can promote the stabilization of mononuclear entities, like in the case of former, in both, chiral and non-chiral metallo-porphyrins (**1a** and **2a**, respectively). In addition, **1a** shows a quite distinctive 1D supramolecular structure. Hexane promotes aggregation in the chiral and non-chiral systems, having at the end coordination 1D structures (**1b**) or 2D systems (**2b**), respectively. Regarding the effect of chirality, **1a** and **1b**, exhibit supramolecular and coordinative 1D architectures that differ, but share certain similarities like the disposition of the chromophore units, giving as a result helical chains and the possibility of analyzing the systems by additional techniques (as CD) in the solid state. The achiral versions lack for this type of rearrangements.

On the topic of chirality, CD and VCD solid-state experiments presented differences between **1a** and **1b**, stressing their sensitivity as well, although the variations in the former were not intuitive and difficult to understand without the assistance of the crystallographic data. In the case of the second, it presented relevant changes in the area related to the C=O stretching, in agreement with the coordination to Zn atoms. Yet, our results emphasize that the proper analysis of the structures by the exclusive use

of such techniques requires the creation of extended libraries and corroboration from theoretical calculations.

Finally, the studies of our systems on two different substrates show the enormous effect of the surfaces on the final structures, providing a variety of vesicles, flower-shapes and well defined geometrical architectures, increasing at times the capacity of achieving microcrystals (e.g.: **2b** in graphite). Here again, chirality should be underlined due to the differences found between the chiral and achiral systems under the same conditions.

Our studies show all the factors that lead supramolecular design: metallo-coordination, chirality, nature of solvents and surfaces; play relevant roles; however, they also provide fingerprints that repeat (e.g.: coordinative-bindings, supramolecular chirality, shapes on surfaces,…) being of great relevance the creation of libraries with extended studies as the present here. The realistic application of molecular materials will undergoes through their disposal on substrates in the solid state. The understanding of the supramolecular nature is vital for future uses in several fields, as for example photovoltaics, that will benefit from such knowledge.

Experimental Section

Materials and Methods. Experiments were carried out in aerobic conditions or under N_2 atmosphere when required, using commercial grade solvents for the synthesis of the four crystallographic species. Solvents were dried and distilled for some of the synthetic steps and for the absorption UV-Vis studies. Methyl (4-formylphenoxy) acetate was purchased in Activate Scientific. (R)-methyl-2-(4-formyl phenoxy)-propionate was achieved by modifying prior procedure improving the yield.[14] 5,10,15,20-tetra[(4-R,R,R,R)-methyl-2-phenoxy-propanoate]-porphyrin, here described as 4R-H_2PPP, was synthesized according to the procedure described elsewhere.[10]

Synthesis. *Synthesis of 5,10,15,20-tetra[(4-R,R,R,R)-methyl-2-phenoxy-propanoate]-porphyrin, (4R-H₂PPP)*. Freshly distilled pyrrole (810 µL, 11.53 mmol) was mixed with 4-formylphenoxy propanoate (2.4 g, 11.53 mmol) and refluxed during 2 h using propionic acid as solvent (42 mL). After the vacuum distillation of propionic acid, the remaining dark viscous solid was washed with a saturated sodium

carbonate solution to remove residual acid. The free-base porphyrin (4R-H$_2$PPP) was then isolated as a purple solid after purification by column chromatography (SiO$_2$, CH$_2$Cl$_2$/CH$_3$OH 100:0.5)[15]. Yield: 790 mg (27 %). Anal. calcd for C$_{60}$H$_{54}$N$_4$O$_{12}$ (1023.09 g·mol^{-1}): C 70.44; H 5.32; N 5.48. Found: C 70.57; H 5.27; N 5.39. ^{1}H NMR (300 MHz, CDCl$_3$, 25 °C): ^{1}H NMR (300 MHz, CDCl$_3$, 25 °C): δ 8.84 (s, 8H), 8.10 (d, J = 8.7 Hz, 8H), 7.24 (d, J = 8.7 Hz, 8H), 5.23 – 4.95 (m, 4H), 3.93 (s, 12H), 1.83 (d, J = 6.8 Hz, 12H), -2.80 (s, 2H). ATR-FTIR date (cm^{-1}): 3319(w), 2925(w), 1755(s), 1739(s), 1605(m), 1504(m), 1133(s), 967(m), 736(w). Maldi-TOF/MS m/z (%): 1022.68 ([4R-H$_2$PPP]$^+$).

Synthesis of [Zn(OH$_2$)(4R-PPP)] (1a). 4R-H$_2$PPP (300 mg, 293 µmol) was dissolved and refluxed in 40 mL of CH$_2$Cl$_2$ under N$_2$ atmosphere. A solution of Zn(CH$_3$COO)$_2$·2H$_2$O (220 mg, 1 mmol) in a mixture of CH$_3$OH/CH$_2$Cl$_2$ (10 ml:10 ml) was added drop wise. The reaction was monitored by absorption UV-Vis spectroscopy (~ 3 h). Afterward, the final solution was washed with NaHCO$_3$ saturated aqueous solution, brine and distilled water. The organic phase was extracted using CH$_2$Cl$_2$. The removal of the solvent gave the desired product as a shining purple solid.[17] Yield: 278 mg (86 %). Suitable crystals for X-ray diffraction analyses of **1a** were achieved after few days by dissolving the solid in a 1:1 mixture of CH$_2$Cl$_2$ and CH$_3$OH, leaving the final solution open to air. Anal. calcd for C$_{60}$H$_{54}$N$_4$O$_{13}$Zn·0.45H$_2$O: C 64.77; H 4.97; N 5.04. Found: C 64.64; H 4.80; N 4.94. ATR-FTIR date (cm^{-1}): 3642(w), 3478(w), 2989(w), 1751(s), 1733(s), 1605(m), 1505(s), 1488(s), 1445(m), 1338(m), 1277(m), 1203(s), 1172(s), 1129(s), 995(s), 846(m), 795(s). Maldi-TOF/MS m/z (%): 1084.62 ([Zn(4R-PPP)]$^+$).

Synthesis of [Zn(4R-PPP)]$_n$ (1b). **1b** was achieved by following previous procedure but using dehydrated Zn(CH$_3$COO)$_2$. Yield: 277 mg (86 %). Crystals of **1b** were achieved by dissolving the final solid in CH$_2$Cl$_2$ and layering the solution with C$_6$H$_{14}$. Anal. calcd for C$_{60}$H$_{52}$ZnN$_4$O$_{12}$ (1086.45 g·mol^{-1}): C 66.33; H 4.82; N 5.16. Found: C 66.61; H 5.07; N 5.02. ATR-FTIR date cm^{-1}): 2988(w), 1757(s), 1739(s), 1721(s), 1605(m), 1506(s), 1445(m), 1340(m), 1201(s), 1176(s), 1131(s), 996(s), 799(s). Maldi-TOF/MS m/z (%): 1084.63 ([Zn(4R-PPP)]$^+$).

Synthesis of H$_2$PPP. Freshly distilled pyrrole (800 µL, 11.53 mmol) was mixed with methyl (4-formylphenoxy) acetate (2.239 g, 11.53 mmol) in refluxing propionic acid (42 mL). After 2 h, propionic acid was removed by vacuum distillation. The dark viscous material that remained was washed with saturated sodium carbonate solution. The free-base porphyrin (H$_2$PPP) was isolated as a purple solid

(723 mg, 26 %) after purification by column chromatography (SiO$_2$, CH$_2$Cl$_2$/ CH$_3$OH 100:0.5). Anal. calcd for C$_{56}$H$_{46}$N$_4$O$_{12}$ (966.98 g·mol^{-1}): C 69.56; H 4.79; N 5.79. Found: C 69.45; H 4.67; N 5.64. ^{1}H NMR (300 MHz, CDCl$_3$, 25 °C): δ 8.85 (s, 8H), 8.13 (d, J = 8.5 Hz, 8H), 7.29 (d, J = 8.5 Hz, 8H), 4.94 (s, 8H), 3.95 (s, 12H), -2.79 (s, 2H). ATR-FTIR date (cm^{-1}): 3650(w), 2954(m), 1753(s), 1604(m), 1507(m), 1219(s), 1170(s), 1084(m), 997(w), 966(w), 802(m) Maldi-TOF/MS m/z (%): 966.22 ([H$_2$PPP]$^+$).

Synthesis of [Zn(PPP)] (2a). The procedure was identical to that described in **1a** but using H$_2$PPP. Yield: 249 mg (78 %). Crystals of **2a** were achieved as for **1a**. Anal. calcd for C$_{56}$H$_{44}$N$_4$O$_{12}$Zn·1.85H$_2$O: C 63.23; H 4.52; N 5.27. Found: C 63.01; H 4.29; N 5.07. ATR-FTIR date (cm^{-1}): 3347(w), 2851(w), 1752(s), 1606(m), 1509(s), 1434(m), 1284(w), 1217(s), 1204(s), 1171(s), 1084(s), 997(s), 799(s), 717(m). Maldi-TOF/MS m/z (%): 1028.15 ([Zn(PPP)]$^+$).

Synthesis of [Zn(PPP)]$_n$ (2b). The procedure was as described for **2a** but using H$_2$PPP. Crystals of **2b** were achieved by following the procedure described in **1b**. Crystallographic data was pursued and shown below. Further analyses were unfeasible due to the scarce amount of the crystalline samples.

Physical Measurements. C, H and N analyses were performed with a Perkin-Elmer 2400 series II analyser in London Metropolitan University and Thermo Fisher Scientific Flash EA 2000 CHNS with accessory Microbalança MX5 Mettler Toledo in Servei d'Anàlisi Química in UAB. Correlation of the experimental data was performed with the use of http://www.chem.yorku.ca/profs/potvin/Jasper/jasper2.htm. Simultaneous thermogravimetric analysis (TG)-differential scanning calorimetry/ differential thermal analysis (heat flow DSC/DTA) system NETZSCH -STA 449 F1 Jupiter. MALDI-TOF/TOF MS: Mass spectra were recorded using matrix assisted laser desorption ionization with time of flight (MALDI-TOF) mass spectrometer ULTRAFLEXTREME (Bruker) at Servei de Proteòmica i Biologia Estructural (SePBioEs) from UAB. FTIR: Infrared spectra (4000-450 cm^{-1}) were recorded from Spectrometer Perkin-Elmer Spectrum One. The measurement was performed in universal attenuated NMR spectra: ^{1}H-NMR spectra were obtained on Bruker Advanced at 300 MHz and 298 K. The ^{13}C-NMR spectra were recorded using frequency 100 MHz in the Servei de Ressonància Magnètica of the Universitat Autònoma de Barcelona, performed on a Bruker AVANCE-III 400 MHz spectrometer. UV-Visible absorption measurements: All UV-visible spectra for liquid samples were obtained on a Varian Cary 5000 using quartz cells. For solid samples it is avail-

able a Diffuse Reflectance Sphere DRA-2500 accessory in the UV-Vis-NIR Varian Cary 5000 spectrophotometer, with operational range of 190-3300 nm, and be measured mainly in reflectance or transmittance mode. Powder X-ray diffraction (PXRD): Dates were collected on Panalytical X'PERT PRO MPD diffractometer using Cu K α radiation at 295K. CD: KBr discs were used as the solid solution for the study of circular dichroism spectra. The solid-state circular dichroism spectra were recorded on a JASCO-715 spectrometer fitted with a sample holder. For vibrational circular dichroism (VCD), the equipment is a PMA50 module coupled to a Bruker Tensor 27 FT-IR spectrometer. Investigation of morphology and surface self-organization phenomena were performed on Luminescence spectrometer Perkin Elmer LS4 and Scanning Electron Microscope (SEM) QUANTA FEI 200 FEG-ESEM. Atomic force microscopy (AFM) contact mode measurements were carried out at room temperature using a commercial head and control unit from Nanotec Electrónica and Si tips mounted in soft (k ≈ 0.01-0.5 Nm^{-1}) Veeco cantilevers. All data were analysed with the WSxM freeware.[42]

Single crystal X-ray diffraction. Crystallographic data for **1a** were measured on a Nonius Kappa CCD diffractometer with graphite monochromatic Mo-radiation (λ = 0.71073 Å) at 233 K and used in the structure solution and refinement with the SHELXTL 5.10 package[43] without absorption correction. Hydrogen atoms at the coordinated water molecule O(13) were found and refined with bond restraints (d = 0.83Å) and fixed isotropic thermal parameter (1.2 times higher than Ueq of O(13). The absolute structure of the compound could be confirmed by a Flack parameter of 0.003(10). Crystallographic data for **1b,2a** and **2b** were collected at 100K at XALOC beamline at ALBA synchrotron (λ = 0.97472 Å for **1b** and 0.79472 Å for **2a** and **2b**). Data were indexed, integrated and scaled using the XDS[44] and IMOSFLM[45] programs. Absorption corrections were not applied. The structures were solved by direct methods and subsequently refined by correction of F^2 against all reflections, using SHELXS2013[46] and SHELXL2013[47] within the WinGX package.[48] All non-hydrogen atoms were refined with anisotropic thermal parameters by full-matrix least-squares calculations on F^2 using the program SHELXL2013. Hydrogen atoms were inserted at calculated positions and constrained with isotropic thermal parameters. Some reflections (2 in **2a** and 6 in **2b**) were omitted from the refinement due to the Iobs and Icalc differ more than 10 times SigmaW. In **1b** and **2a**, the low data completeness is attributed to the data collection having been performed with only omega scan. This feature is also reflected in the low value of the refined Flack parameter in **1b** (-0.264(5)) but, although this value does not permit

unambiguous determination of the absolute structure; its absolute configuration is established by reference to an unchanging chiral centre in the synthetic procedure.

Acknowledgements

References

[1] M. Fujita, *Chem. Soc. Rev.* **1998**, *27*, 417-425.

[2] J. E. Raymond, A. Bhaskar, T. Goodson III, N. Makiuchi, K. Ogawa and Y. Kobuke, *J. Am. Chem. Soc.* **2008**, *130*, 17212-17213.

[3] G. M. Whitesides and B. Grzybowski, *Science* **2002**, *295*, 2418-2421.

[4] D. J. McClements, *Biotechnol. Adv.* **2006**, *24*, 621-625.

[5] E. R. Johnson, S. Keinan, P. Mori-Sanchez, J. Contreras-Garcia, A. J. Cohen and W. Yang, *J. Am. Chem. Soc.* **2010**, *132*, 6498-6506.

[6] J. Shelnutt and C. Medforth, *Chem. Soc. Rev.* **1998**, *27*, 31-42.

[7] F. J. Hoeben, M. Wolffs, J. Zhang, S. De Feyter, P. Leclère, A. P. Schenning and E. Meijer, *J. Am. Chem. Soc.* **2007**, *129*, 9819-9828.

[8] S. A. Rousseaux, J. Q. Gong, R. e. Haver, B. Odell, T. D. Claridge, L. M. Herz and H. L. Anderson, *J. Am. Chem. Soc.* **2015**, *137*, 12713-12718.

[9] O. Shoji, S. Okada, A. Satake and Y. Kobuke, *J. Am. Chem. Soc.* **2005**, *127*, 2201-2210.

[10] C. Oliveras-González, F. Di Meo, A. n. González-Campo, D. Beljonne, P. Norman, M. Simón-Sorbed, M. Linares and D. B. Amabilino, *J. Am. Chem. Soc* **2015**, *137*, 15795-15808.

[11] P. Iavicoli, H. Xu, L. N. Feldborg, M. Linares, M. Paradinas, S. Stafström, C. Ocal, B. Nieto-Ortega, J. Casado and J. T. Lopez Navarrete, *J. Am. Chem. Soc.* **2010**, *132*, 9350-9362.

[12] F. Helmich, C. C. Lee, A. P. Schenning and E. Meijer, *J. Am. Chem. Soc.* **2010**, *132*, 16753-16755.

[13] E. Bellacchio, R. Lauceri, S. Gurrieri, L. M. Scolaro, A. Romeo and R. Purrello, *J. Am. Chem. Soc.* **1998**, *120*, 12353-12354.

[14] M. Minguet, D. B. Amabilino, J. Vidal-Gancedo, K. Wurst and J. Veciana, *J. Mater. Chem.* **2002**, *12*, 570-578.

[15] M. Linares, P. Iavicoli, K. Psychogyiopoulou, D. Beljonne, S. De Feyter, D. B. Amabilino and R. Lazzaroni, *Langmuir* **2008**, *24*, 9566-9574.

[16] P. Iavicoli, M. Linares, A. P. del Pino, R. Lazzaroni and D. B. Amabilino, *Superlattices Microstruct.* **2008**, *44*, 556-562.

[17] L. N. Feldborg, W. J. Saletra, P. Iavicoli and D. B. Amabilino, *J. Porphyr. Phthalocyanines* **2011**, *15*, 995-1003.

[18] A. Wakisaka, S. Komatsu and Y. Usui, *J. Mol. Liq.* **2001**, *90*, 175-184.

[19] D. Monti, M. De Rossi, A. Sorrenti, G. Laguzzi, E. Gatto, M. Stefanelli, M. Venanzi, L. Luvidi, G. Mancini and R. Paolesse, *Chem. Eur. J.* **2010**, *16*, 860-870.

[20] X. Rui, Q.-Z. Zha, T.-T. Wei and Y.-S. Xie, *Inorg. Chem.Commun.* **2014**, *48*, 111-113.

[21] E. B. Fleischer and A. M. Shachter, *Inorg. Chem.* **1991**, *30*, 3763-3769.

[22] A. Huijser, B. M. Suijkerbuijk, R. J. Klein Gebbink, T. J. Savenije and L. D. Siebbeles, *J. Am. Chem. Soc.* **2008**, *130*, 2485-2492.

[23] T.-L. Teo, M. Vetrichelvan and Y.-H. Lai, *Org. lett.* **2003**, *5*, 4207-4210.

[24] F. Zsila, Z. Bikádi, I. Fitos and M. Simonyi, *Curr. Drug Discov.Technol.* **2004**, *1*, 133-153.

[25] S. Dugar, R. Fu and N. S. Dalal, *J. Phys. Chem. B* **2012**, *116*, 9215-9222.

[26] M. Strohmeier, A. M. Orendt, J. C. Facelli, M. S. Solum, R. J. Pugmire, R. W. Parry and D. M. Grant, *J. Am. Chem. Soc.* **1997**, *119*, 7114-7120.

[27] N. Bampos, M. R. Prinsep, H. He, A. Vidal-Ferran, A. Bashall, M. McPartlin, H. Powell and J. K. Sanders, *J. Chem. Soc, Perkin Trans. 2* **1998**, 715-724.

[28] M. Minguet, D. B. Amabilino, K. Wurst and J. Veciana, *J. Chem. Soc, Perkin Trans. 2* **2001**, 670-676.

[29] E. Castiglioni, P. Biscarini and S. Abbate, *Chirality* **2009**, *21*.

[30] S. K. Avula, H. Hussain, R. Csuk, S. Sommerwerk, P. Liebing, M. Górecki, G. Pescitelli, A. Al-Rawahi, N. U. Rehman and I. R. Green, *Tetrahedron: Asymmetry* **2016**, *27*, 829-833.

[31] G. A. Hembury, V. V. Borovkov and Y. Inoue, *Chem. Rev.* **2008**, *108*, 1-73.

[32] C.-Y. Zheng and H. Li, *Inorg. Chem.Commun.* **2013**, *34*, 30-33.

[33] J. Frelek, M. Górecki, M. Łaszcz, A. Suszczyńska, E. Vass and W. J. Szczepek, *Chem.Commun.* **2012**, *48*, 5295-5297.

[34] A. D. Becke, *J. Chem. Phys.* **1993**, *98*, 5648-5652.

[35] M. J. Frisch, G. W. Trucks, H. B. Schlegel, G. E. Scuseria, M. A. Robb, J. R. Cheeseman, G. Scalmani, V. Barone, B. Mennucci, G. A. Petersson, H. Nakatsuji, M. Caricato, X. Li, H. P. Hratchian, A. F. Izmaylov, J. Bloino, G. Zheng, J. L. Sonnenberg, M. Hada, M. Ehara, K. Toyota, R. Fukuda, J. Hasegawa, M. Ishida, T. Nakajima, Y. Honda, O. Kitao, H. Nakai, T. Vreven, J. Montgomery, J. A., J. E. Peralta, F. Ogliaro, M. Bearpark, J. J. Heyd, E. Brothers, K. N. Kudin, V. N. Staroverov, R. Kobayashi, J. Normand, K. Raghavachari, A. Rendell, J. C. Burant, S. S. Iyengar, J. Tomasi, M. Cossi, N. Rega, N. J. Millam, M. Klene, J. E. Knox, J. B. Cross, V. Bakken, C. Adamo, J. Jaramillo, R. Gomperts, R. E. Stratmann, O. Yazyev, A. J. Austin, R. Cammi, C. Pomelli, J. W. Ochterski, R. L. Martin, K. Morokuma, V. G. Zakrzewski, G. A. Voth, P. Salvador, J. J. Dannenberg, S. Dapprich, A. D. Daniels, Ö. Farkas, J. B. Foresman, J. V. Ortiz, J. Cioslowski and D. J. Fox in *Gaussian 09 (Revision D.01)*, *Vol.* Wallingford, CT, **2009**.

[36] N. Jiang, R. X. Tan and J. Ma, *J. Phys. Chem. B* **2011**, *115*, 2801-2813.

[37] C. Huang, Y. Li, J. e. Yang, N. Cheng, H. Liu and Y. Li, *Chem. Commun.* **2010**, *46*, 3161-3163.

[38] M. Morisue, T. Morita and Y. Kuroda, *Org. Biomol. Chem.* **2010**, *8*, 3457-3463.

[39] S.-i. Tamaru, M. Nakamura, M. Takeuchi and S. Shinkai, *Org. Lett.* **2001**, *3*, 3631-3634.

[40] T. Wang, S. Chen, F. Jin, J. Cai, L. Cui, Y. Zheng, J. Wang, Y. Song and L. Jiang, *Chem. Commun.* **2015**, *51*, 1367-1370.

[41] J. Lu, D. Zhang, H. Wang, J. Jiang and X. Zhang, *Inorg. Chem.Commun.* **2010**, *13*, 1144-1147.

[42] I. Horcas, R. Fernández, J. Gomez-Rodriguez, J. Colchero, J. Gómez-Herrero and A. Baro, *Rev. Sci. Instrum.* **2007**, *78*, 013705.

[43] S. Bruker, *Bruker Analytical X-ray Instruments Inc., Madison, WI, USA* **1997**.

[44] W. Kabsch, *Acta Crystallogr. Sect. D-Biol. Crystallogr.* **2010**, *66*, 133-144.

[45] A. G. Leslie, *Acta Crystallogr. Sect. D-Biol. Crystallogr.* **2006**, *62*, 48-57.

[46] G. M. Sheldrick, Z. Dauter, K. Wilson, H. Hope and L. Sieker, *Acta Crystallogr. Sect. D-Biol. Crystallogr.* **1993**, *49*, 18-23.

[47] G. M. Sheldrick, *Acta Crystallogr. Sect. C-Cryst. Struct. Commun.***2015**, *71*, 3-8.

[48] L. J. Farrugia, *J. Appl. Crystallogr.* **2012**, *45*, 849-854.

SUPPLEMENTARY INFORMATION

Figures and Tables

Scheme S1. General description of the methodology followed to re-crystallise **1a, 1b**, **2a** and **2b**.

Table S1. Crystal and Experimental Data for Structures **1a**, **1b**, **2a** and **2b**.

Table S2. Selected bond lengths [Å] and angles [°] for **1a**.

Table S3. Selected bond lengths [Å] and angles [°] for **1b**.

Table S4. Selected bond lengths [Å] and angles [°] for **2a**.

Table S5. Selected bond lengths [Å] and angles [°] for **2b**.

Table S6. Absorption maxima of the UV/Vis spectra of Zn porphyrins.

Figure S1. IR of 4R-H$_2$PPP and H$_2$PPP.

Figure S2. ^{1}H-NMR of 4R-H$_2$PPP and H$_2$PPP.

Figure S3. Microscope images of crystals.

Figure S4. Different crystallographic projections of **1a**.

Figure S5. Different crystallographic projections of **1b**.

Figure S6. Different crystallographic projections of **2a**.

Figure S7. Different crystallographic projections of **2b**.

Figure S8. 2D supramolecular organization of **1a**.

Figure S9. 3D supramolecular organization of **1a**.

Figure S10. 3D supramolecular organization of **2b**.

Figure S11. Coordinative 1D system of **1b**.

Figure S12. NMR of **1a** in different concentration in CDCl$_3$.

Figure S13. NMR of **1b** in different concentration in CDCl$_3$.

Figure S14. UV-Vis absorption spectroscopy of Zn-porphyrins.

Figure S15. XRD of crystal collected in different conditions to analyse the origin of the coordinated H$_2$O molecule in **1a**.

Figure S16-19. PXRD profiles of **1a, 1b**, **2a** and **2b**.

Figure S20. ATR-FTIR of **1a** and **1b**.

Figure S21. ATR-FTIR of **2a**.

Figure S22. TGA graphs for **1a**, **1b** and **2a**, respectively.

Figure S23. The solid-state ^{13}C NMR spectra of 4*R*-H$_2$PPP between 180 – 0 ppm.

Figure S24. The solid-state UV-Vis of **1a**, **1b** and **2a** crystals.

Figure S25-27. Solid-state CD spectra of compounds **1a**, **1b** and **2a**.

Figure S28. UV-Vis absorption spectroscopy of Zn-porphyrin in CH$_2$Cl$_2$ (top). The solid-state UV-Vis of **1a**, **1b** and **2a** crystals (middle). Solid state CD spectra of **1a**, **1b** and **2a** (down).

Figure S29. Solid state VCD spectra of **2a**.

Figure S30. Theoretical calculation solid state VCD and IR spectra of **1a** and Cartesian coordinates of the DFT optimised structure of **1a**.

Figure S31-40. SEM images of **1** and **2** on surface.
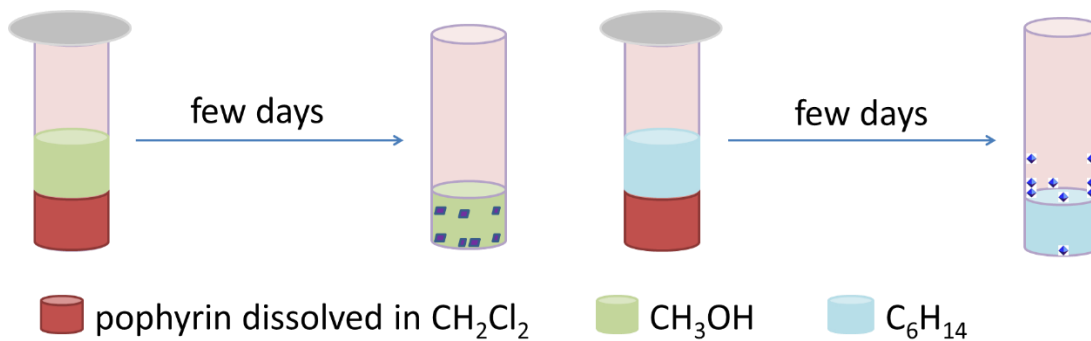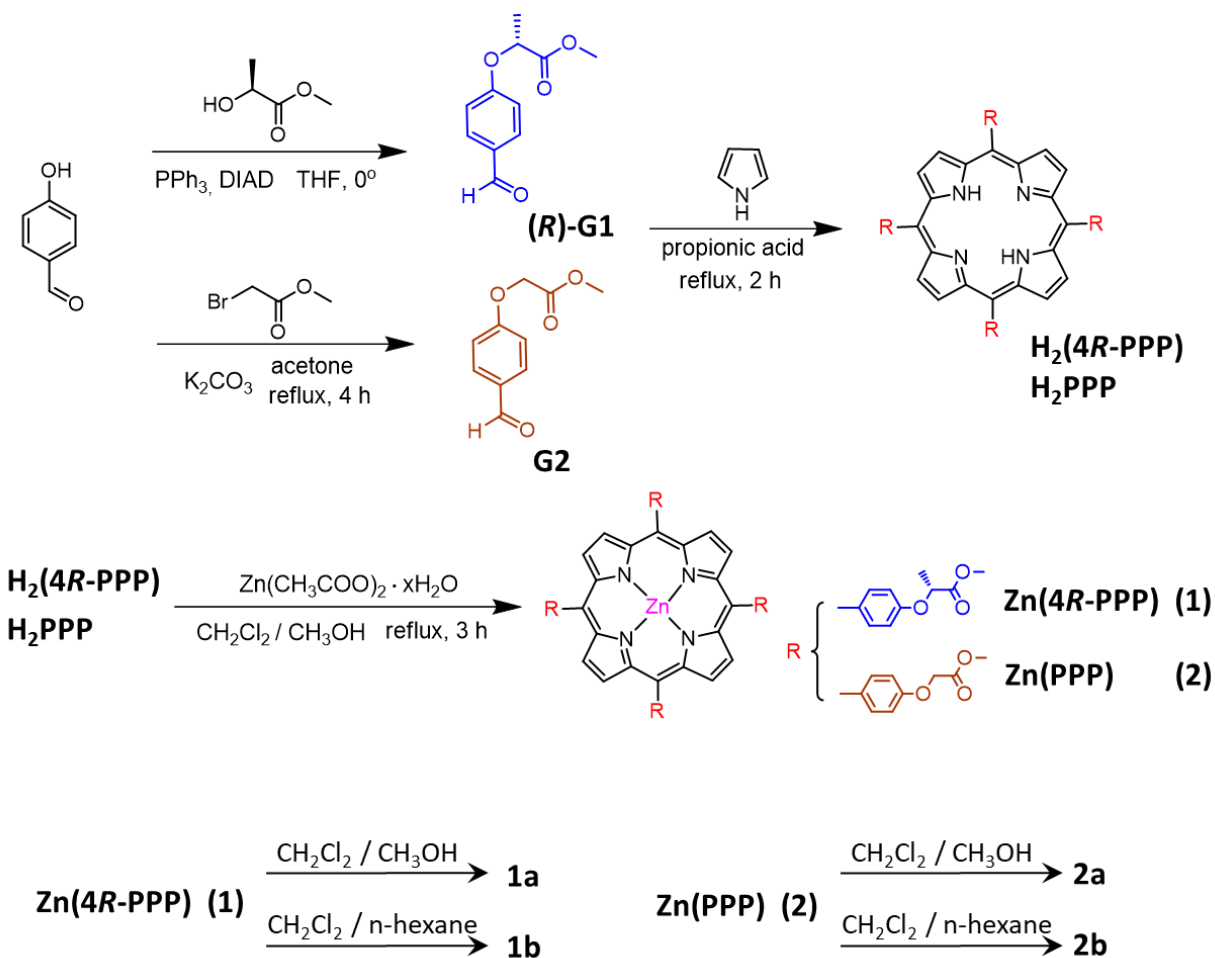
Scheme S1. (Top) Synthesis and crystallization procedure of metalloporphyrins **Zn(4R-PPP)** and **Zn(PPP)** (**1** and **2**) (Bottom) General description of the methodology followed to re-crystallise **1a**, **1b**, **2a** and **2b**.

Table S1. Crystal and Experimental Data for Structures **1a**, **1b**, **2a** and **2b**.

	1a	1b	2a	2b
formula	$C_{60}H_{54}N_4O_{13}Zn$	$C_{60}H_{52}N_4O_{12}Zn$	$C_{56}H_{44}N_4O_{12}Zn$	$C_{56}H_{44}N_4O_{12}Zn$
F_w	1104.44	1086.45	1030.34	1030.34
crystal system	orthorhombic	orthorhombic	monoclinic	monoclinic
space group	P 21 21 21	P 21 21 21	C 2/c	C 2/c
a [Å]	9.5790(2)	16.8600(0)	21.71000	20.76000
b [Å]	17.3042(3)	17.7400(0)	15.19000	11.92000
c [Å]	32.6567(6)	17.9100(0)	14.35000	24.59000
α [°]	90.00	90.00	90	90
β [°]	90.00	90.00	104.2600	90.2100
γ [°]	90.00	90.00	90	90
V [A^3]	5413.07(18)	5356.816	4586.458	6084.981
Z	4	4	4	4
ρ_{calcd} [Mg m^{-3}]	1.355	1.347	1.492	1.125
μ [mm^{-1}]	0.524	1.225	0.818	0.617
F(000)	2304	2264	2136	2136
crystal size [mm^3]	0.22 x 0.16 x 0.04	0.13 x 0.12 x 0.10	0.11 x 0.10 x 0.08	
θ_{max} [°]	25.00	33.204	33.9	34.0
refl collected	9520	35749	33299	43301
refl unique	7983	6842	5291	7606
R(int)	0.0451	0.0600	0.030	0.018
Completeness (%)	99.6	72.6		
refl with I > 2σ(I)	9520	6842	5168	7404
refined parameters	713	695	332	332
R_1 [I > 2σ(I)]	0.0400	0.0358	0.0409	0.0633
wR_2 [I > 2σ(I)]	0.0894	0.0912	0.1180	0.2023
R_1 [all data]	0.0541	0.0399	0.0412	0.0628
wR_2 [all data]	0.0941	0.0922	01152	0.1910
$\pm\Delta\rho_{max}$ [e Å^{-3}]	+1.015, -1.017	+0.333, -0.516	+0.67, -0.65	+1.97, -0.70

Table S2. Selected bond lengths [Å] and angles [°] for **1a**.

	[Å]		[°]
Zn(1)-N(4)	2.046(2)	N(4)-Zn(1)-N(2)	168.25(10)
Zn(1)-N(2)	2.052(2)	N(4)-Zn(1)-N(1)	90.08(9)
Zn(1)-N(1)	2.066(2)	N(2)-Zn(1)-N(1)	89.68(8)
Zn(1)-N(3)	2.082(2)	N(4)-Zn(1)-N(3)	89.11(9)
Zn(1)-O(13)	2.248(2)	N(2)-Zn(1)-N(3)	88.82(8)
O(13)-H(1O)	0.828(10)	N(1)-Zn(1)-N(3)	168.71(9)
O(13)-H(2O)	0.897(10)	N(4)-Zn(1)-O(13)	96.39(10)
C(5)-C(21)	1.503(4)	N(2)-Zn(1)-O(13)	95.16(10)
C(10)-C(27)	1.499(4)	N(1)-Zn(1)-O(13)	101.43(9)
C(15)-C(33)	1.504(4)	N(3)-Zn(1)-O(13)	89.85(10)
C(20)-C(39)	1.493(4)	Zn(1)-O(13)-H(1O)	113(3)
C(45)-H(45)	0.9900	Zn(1)-O(13)-H(2O)	122(3)
C(45)-C(46)	1.530(6)	O(1)-C(45)-C(46)	109.3(3)
C(45)-C(47)	1.522(6)	O(4)-C(49)-C(50)	109.0(3)
C(49)-H(49)	0.9900	O(7)-C(53)-C(54)	113.2(3)
C(49)-C(50)	1.517(5)	O(10)-C(57)-C(58)	108.2(2)
C(49)-C(51)	1.520(5)		
C(53)-H(53)	0.9900		
C(53)-C(54)	1.501(5)		
C(53)-C(55)	1.514(5)		
C(57)-H(57)	0.9900		
C(57)-C(58)	1.523(4)		
C(57)-C(59)	1.505(4)		
O(2)-C(46)	1.180(5)		
O(5)-C(50)	1.178(4)		
O(8)-C(54)	1.194(4)		
O(11)-C(58)	1.198(4)		
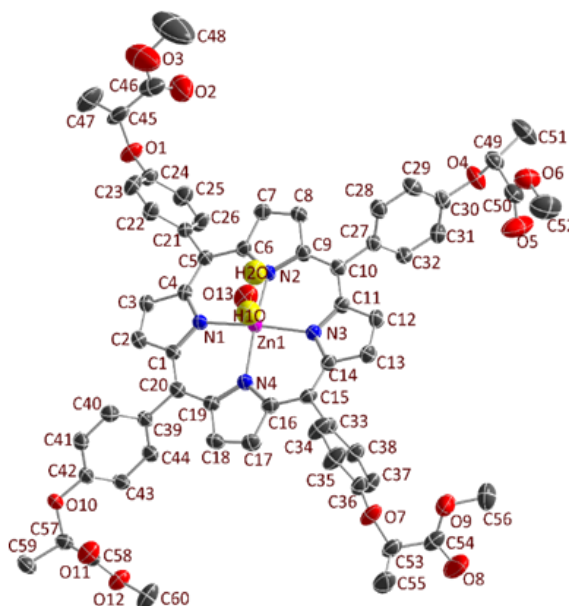
Table S3. Selected bond lengths [Å] and angles [°] for **1b**.

	[Å]		[°]
Zn(1)-N(4)	2.037(3)	N(4)-Zn(1)-N(1)	90.06(13)
Zn(1)-N(1)	2.054(3)	N(4)-Zn(1)-N(2)	169.67(14)
Zn(1)-N(2)	2.057(3)	N(1)-Zn(1)-N(2)	89.00(13)
Zn(1)-N(3)	2.068(4)	N(4)-Zn(1)-N(3)	89.92(14)
Zn(1)-O(5)	2.210(3)	N(1)-Zn(1)-N(3)	169.29(15)
C(2)-C(22)	1.494(6)	N(2)-Zn(1)-N(3)	89.10(13)
C(7)-C(32)	1.496(6)	N(4)-Zn(1)-O(5)	88.72(13)
C(13)-C(42)	1.492(6)	N(1)-Zn(1)-O(5)	104.21(14)
C(18)-C(52)	1.497(6)	N(2)-Zn(1)-O(5)	101.48(13)
C(28)-C(29)	1.481(8)	N(3)-Zn(1)-O(5)	86.50(14)
C(28)-C(30)	1.536(8)	O(1)-C(28)-C(30)	107.9(4)
C(28)- O(1)	1.449(6)	O(4)-C(38)-C(40)	110.8(4)
C(38)-C(39)	1.515(7)	O(7)-C(48)-C(50)	110.4(4)
C(38)-C(40)	1.503(7)	O(10)-C(58)-C(60)	110.6(4)
C(38)- O(4)	1.437(6)		
C(48)-C(49)	1.505(7)		
C(48)-C(50)	1.521(8)		
C(48)- O(7)	1.421(6)		
C(58)-C(59)	1.525(7)		
C(58)-C(60)	1.521(7)		
C(58)- O(10)	1.419(6)		

Table S4. Selected bond lengths [Å] and angles [°] for **2a**.

	[Å]		[°]
Zn(1)-N(1)	2.0365(13)	N(1)-Zn(1)-N(2)	90.06(13)
Zn(1)-N(2)	2.0476(13)	N(1)-Zn(1)-N(1')	180.00
C(2)-C(11)	1.495(2)	N(1)-Zn(1)-N(2')	89.40(5)
C(7)-C(20)	1.496(2)	N(2)-Zn(1)-N(2')	180.00
C(17)-O(1)	1.420(3)	O(1)-C(17)-C(18)	112.34(16)
C(17)-C(18)	1.514(3)	O(4)-C(26)-C(27)	107.56(16)
C(26)-O(4)	1.413(2)		
C(26)-C(27)	1.513(3)		

Table S5. Selected bond lengths [Å] and angles [°] for **2b**.

	[Å]		[°]
Zn(1)-N(1)	2.0466(15)	N(1)-Zn(1)-N(2)	90.41(6)
Zn(1)-N(2)	2.0496(16)	N(1)-Zn(1)-N(1')	180.00
Zn(1)-O(2_b)	2.5102(16)	N(1)-Zn(1)-N(2')	89.59(6)
C(3)-C(11)	1.498(3)	N(2)-Zn(1)-N(2')	180.00
C(8)-C(20)	1.495(3)	N(1)-Zn(1)- O(2_b)	94.37(6)
C(17)-O(1)	1.410(3)	N(1)-Zn(1)- O(2_c)	85.63(6)
C(17)-C(18)	1.510(3)	N(2)-Zn(1)- O(2_b)	95.74(6)
C(26)-O(4)	1.417(3)	N(2)-Zn(1)- O(2_c)	84.26(6)
C(26)-C(27)	1.514(3)	O(2_b)-Zn(1)- O(2_c)	180.00
		O(1)-C(17)-C(18)	115.13(19)
		O(4)-C(26)-C(27)	106.56(17)

Table S6. Absorption maxima of the (Top) solid-state UV/Vis spectra of Zn porphyrins and (Down) UV-Vis absorption spectroscopy of Zn-porphyrins in CH_2Cl_2.

Compound	Soret [nm] (I_{rel})	Q_{vib} [nm] (I_{rel})	Q (I_{rel})
1a	430.0 (1.000)	558.4 (0.603)	598.6 (0.529)
1b	432.2 (1.000)	560.6 (0.554)	600.8 (0.491)
2a	435.0 (1.000)	560.8 (0.511)	600.2 (0.436)

Compound	Soret [nm]	Q_{vib} [nm]	Q [nm]
Zn(4*R*-PPP)	422.2	550	589.4
Zn(PPP)	422.0	549.2	589.8

Figure S1. IR of 4*R*-H$_2$PPP and H$_2$PPP.
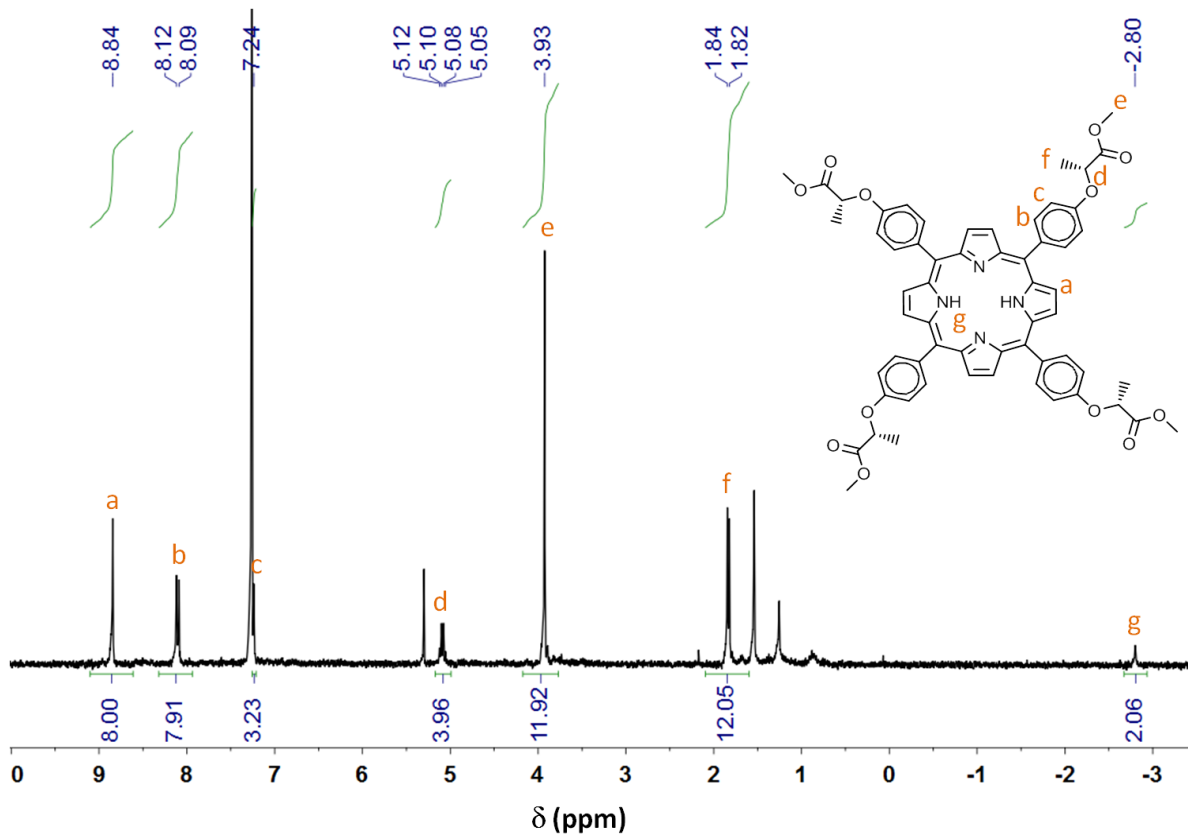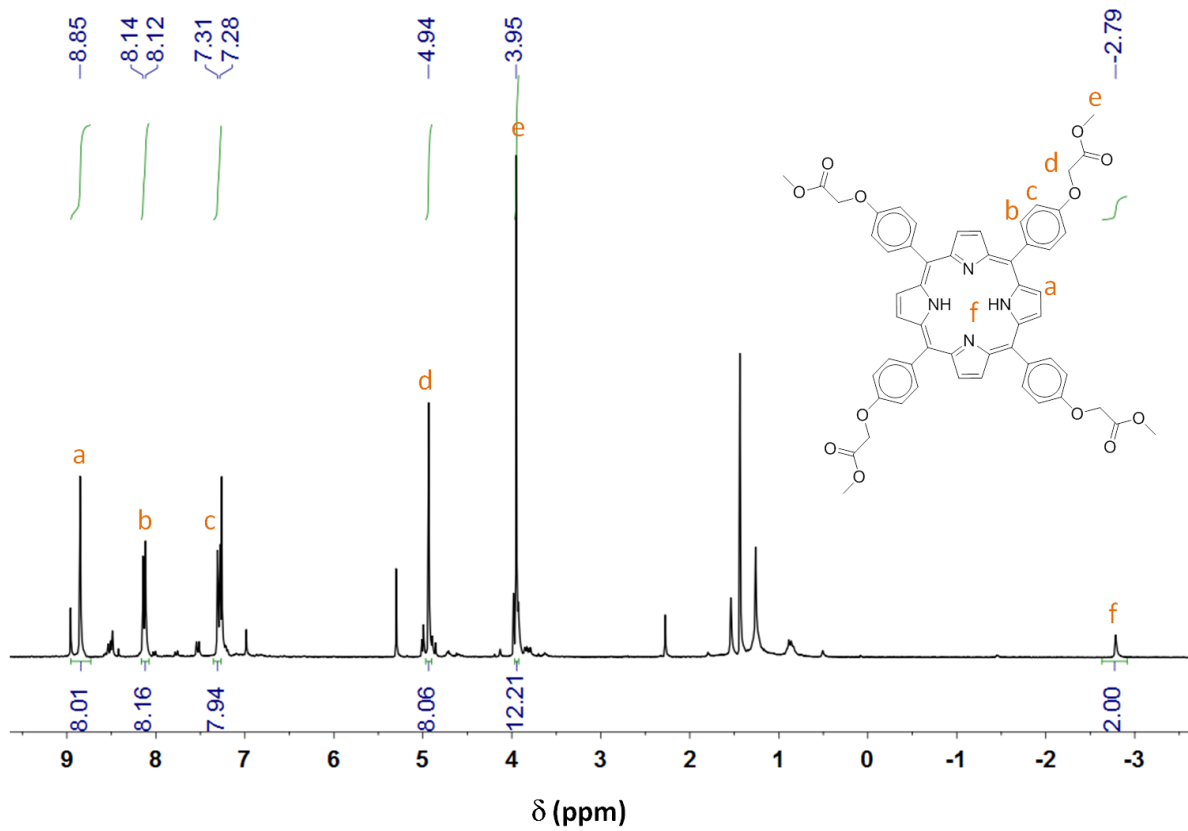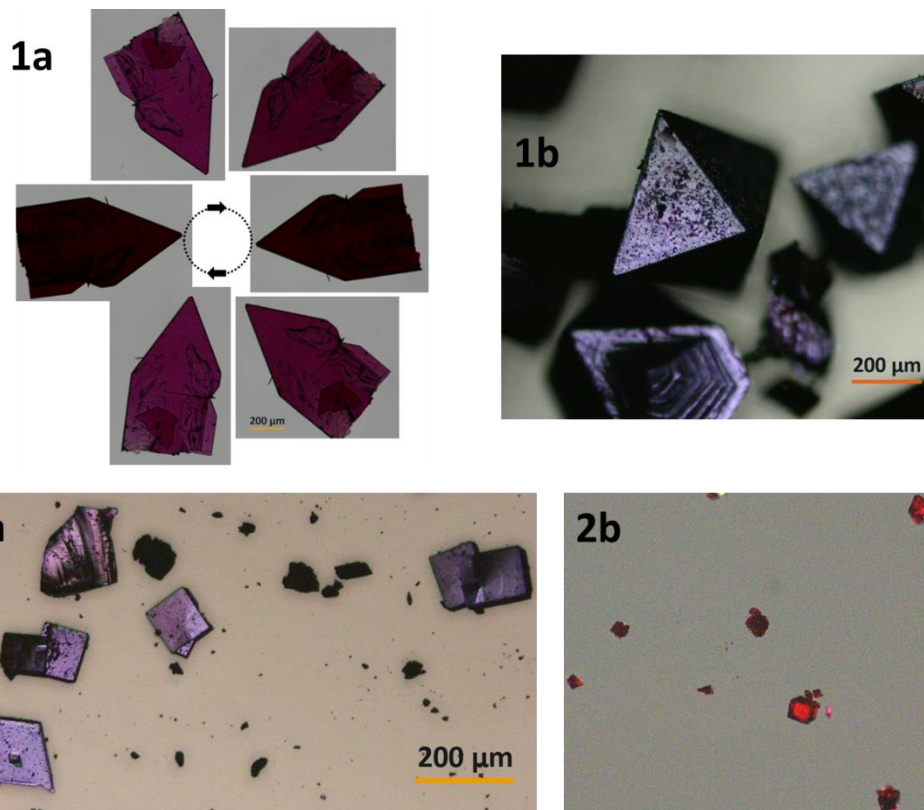
Figure S2. ^{1}H NMR of 4R-H$_2$PPP and H$_2$PPP.

Figure S3. Microscope images of crystals.

Figure S4. Different crystallographic projections of **1a**.
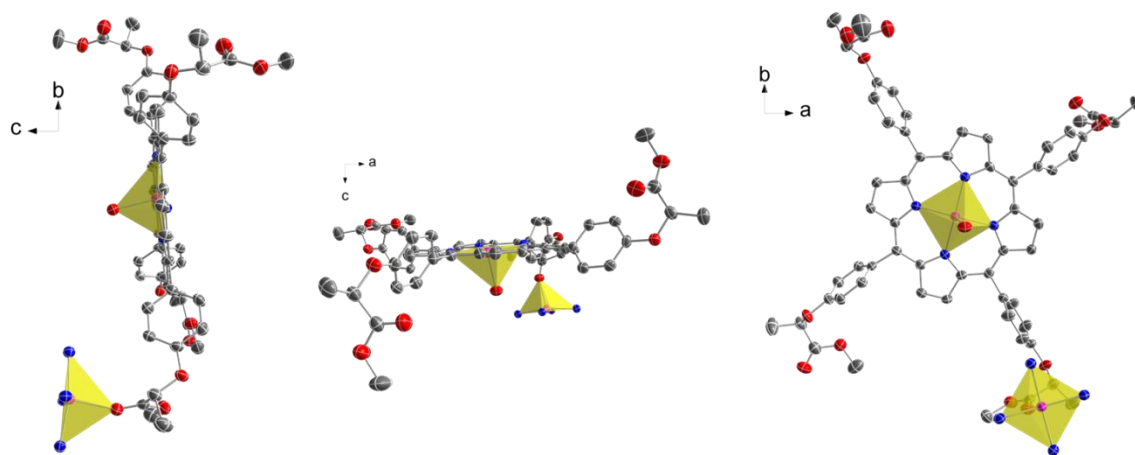
Figure S5. Different crystallographic projections of **1b**.
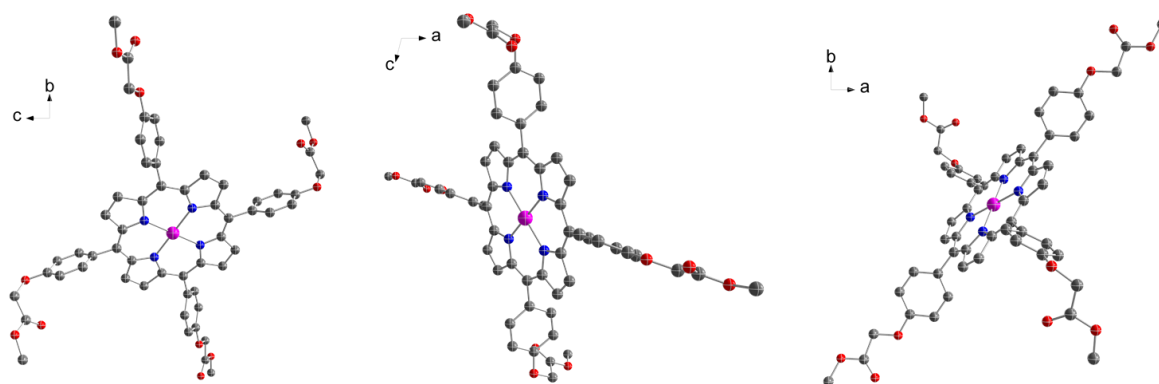
Figure S6. Different crystallographic projections of **2a**.
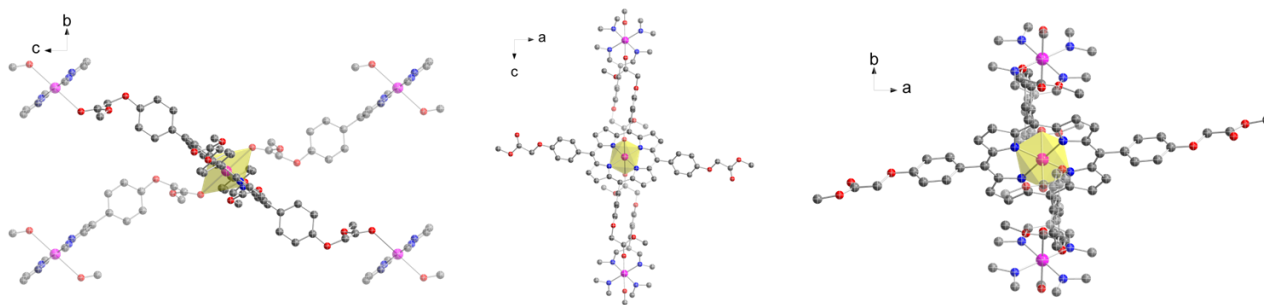
Figure S7. Different crystallographic projections of **2b**.
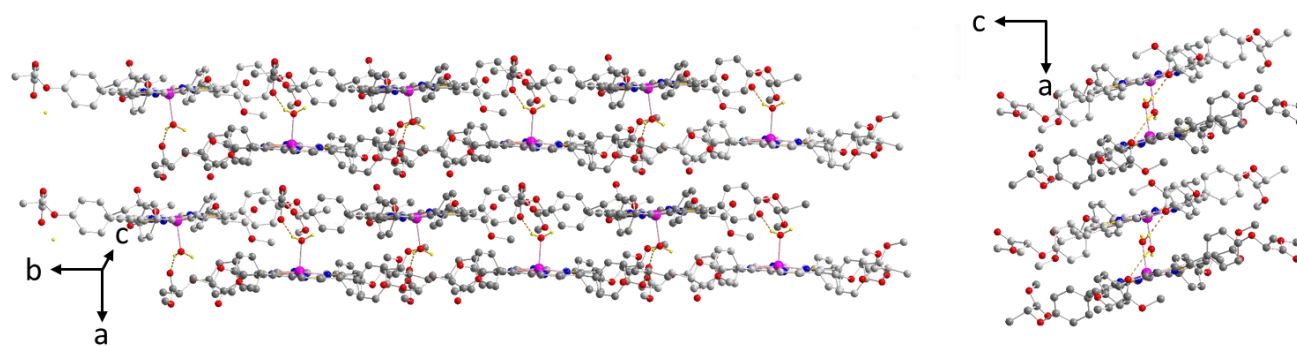
Figure S8. 2D supramolecular organization of **1a**.

Figure S9. 3D supramolecular organization of **1a**.
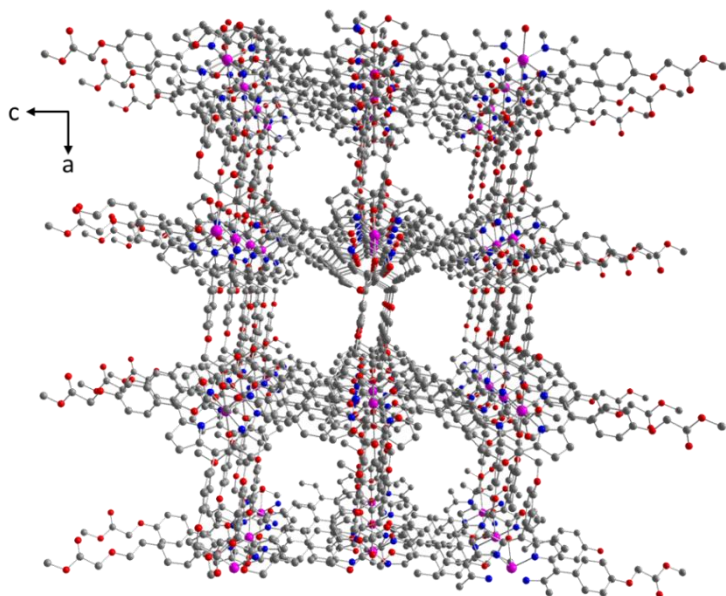
Figure S10. 3D supramolecular organization of **2b**.
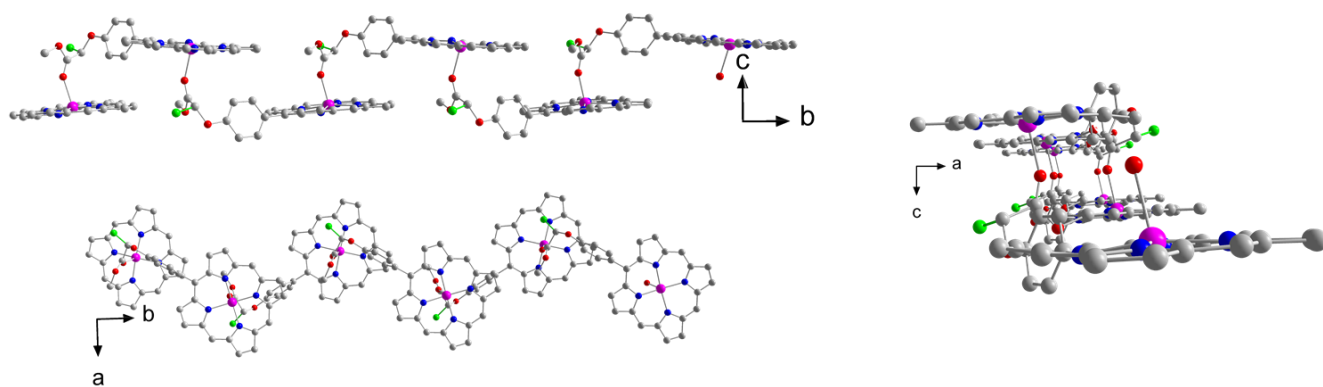
Figure S11. Coordinative 1D system of **1b**. Color legend: Zn in purple, O in red, N in blue, C in gray and −CH$_3$ of the coordinated branch in green.
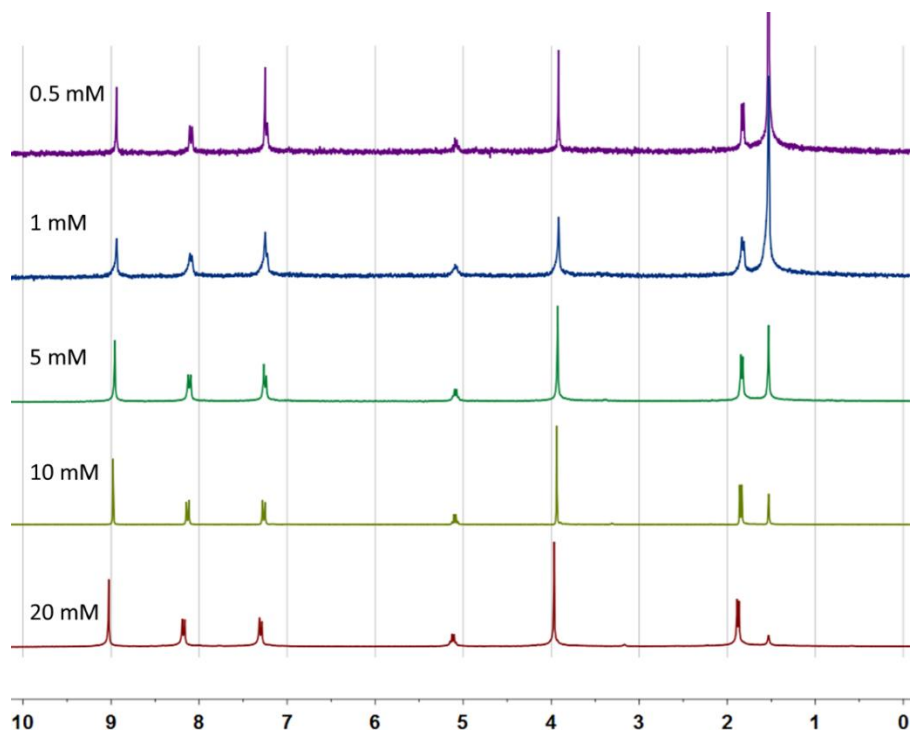
Figure S12. ^{1}H NMR of **1a** in different concentration in CDCl$_3$.
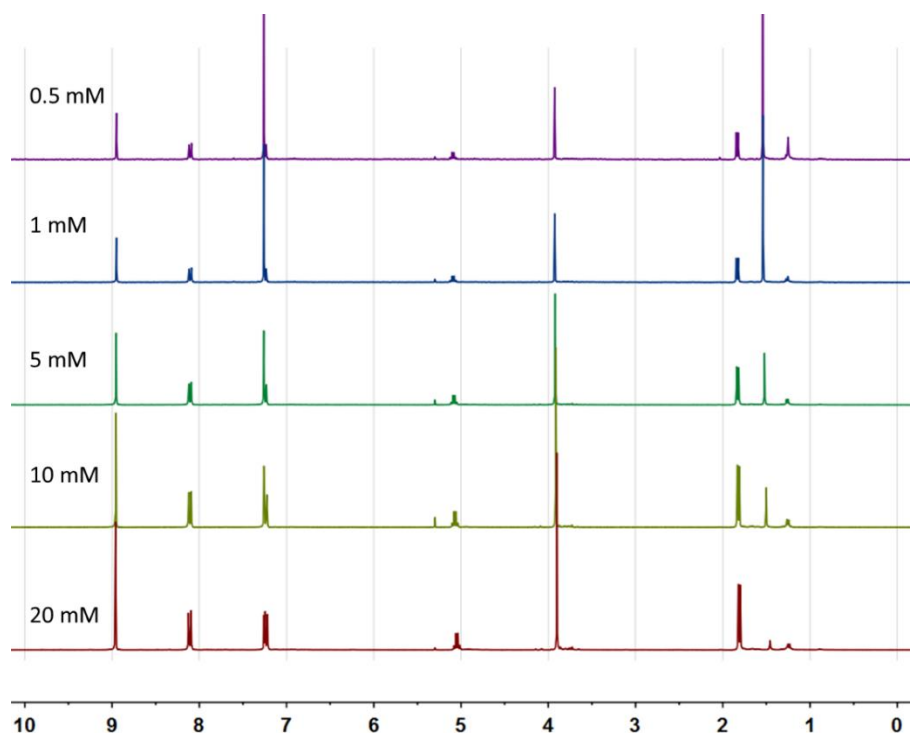
Figure S13. ^{1}H NMR of **1b** in different concentration in CDCl$_3$.
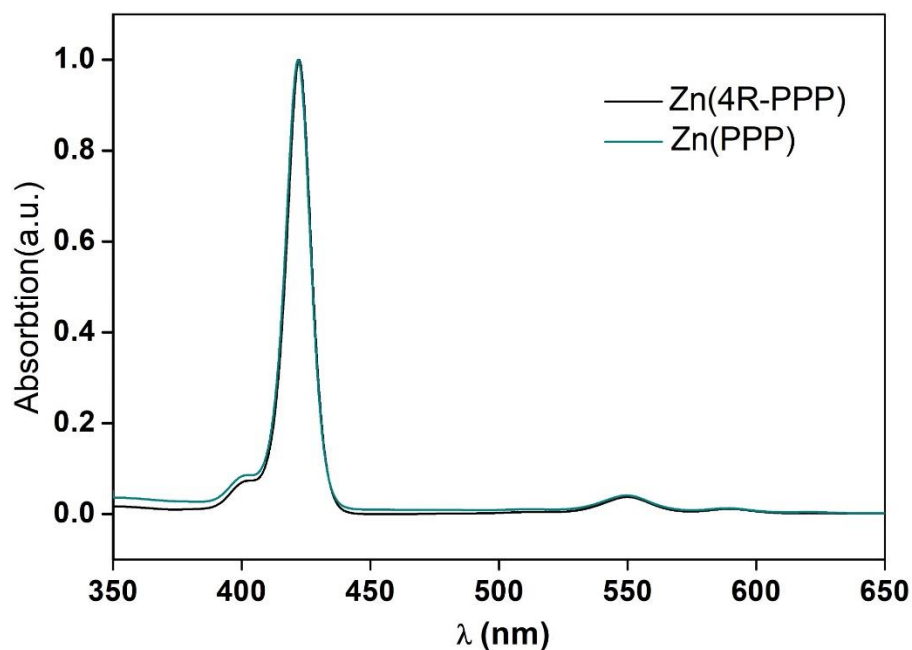
Figure S14. UV-Vis absorption spectroscopy of Zn-porphyrins (**1** and **2**, **Zn(4R-PPP)** and **Zn(PPP)**, respectively) in CH$_2$Cl$_2$.

Study regarding the origin of the coordinated H$_2$O in 1a

1a present Zn(II) centers that are penta-coordinated, where each of them bind to a porphyrin core and to a molecule of H$_2$O, the latest in the apical position. **1a** crystallized from a CH$_2$Cl$_2$/CH$_3$OH mixture; however, there is not CH$_3$OH coordinated to the Zn^{II} ions and furthermore, there are not H$_2$O molecules in the structure of **1b**, achieved from a CH$_2$Cl$_2$/n-hexane mixture, or in **2a**, where identical procedure to that described in **1a** was used. In order to establish the origin of the coordinated H$_2$O molecule in **1a**, we performed a series of experiments varying the source of Zn(II) that are summarized in Table S7. The results of all the studies were analyzed by X-ray powder diffraction, and compared with the simulated graph of **1a**.

Conditions of the experiments.

Compound	Zn[II] used in reaction	Solvent for crystallization
1a	$Zn(CH_3COO)_2 \cdot 2H_2O$	CH_2Cl_2(HPLC)-CH_3OH
1b	$Zn(CH_3COO)_2$	CH_2Cl_2(HPLC)-hexane
C1	$Zn(CH_3COO)_2$	CH_2Cl_2(HPLC)-CH_3OH
C2	$Zn(CH_3COO)_2$	CH_2Cl_2(HPLC)-CH_3OH-H_2O(3 mL)
C3	$Zn(CH_3COO)_2 \cdot 2H_2O$	CH_2Cl_2(HPLC)-hexane
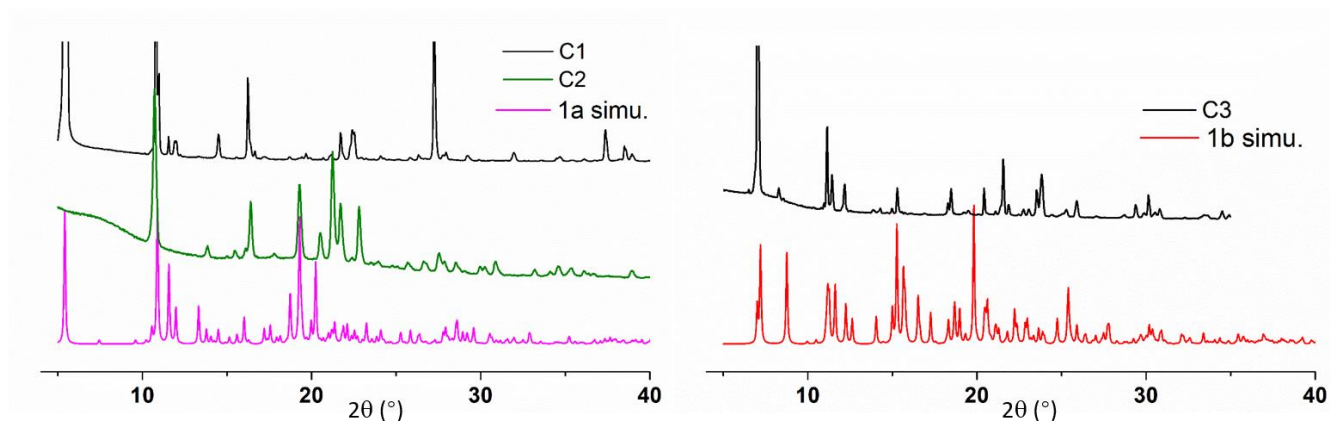
Figure S15. (Left) XRD of **C1** and **C2** comparing with **1a**. (Right) XRD of **C3** comparing with **1b**.

The first modification was performed by the use of dehydrated $Zn(CH_3COO)_2$ using the same crystallographic procedure and materials as for **1a** (CH_2Cl_2(HPLC)/CH_3OH), the resulting sample was named **C1**. The X-ray powder diffraction pattern of C1 (Figure S15) matches well with **1a**. Therefore, our analysis shows that **C1** may also contain the Zn-OH_2 coordination, demonstrating that the H_2O, in **1a**, is not from the $Zn(CH_3COO)_2 \cdot 2H_2O$ source.

In a second test, we used dehydrated $Zn(CH_3COO)_2$, but in the recrystallization process 3 mL of H_2O were added. This step hampered the achievement of good crystals (Figure S15). After the full evaporation of the organic solvent we studied the films floating on the remaining water (here called **C2**). This strategy was taken because CH_3OH is water rich, but in this case, a large amount of H_2O went against the crystallization process.

Finally, $Zn(CH_3COO)_2 \cdot 2H_2O$ was used as the source of metal following the recrystallization method of **1b**, CH_2Cl_2(HPLC)/n-hexane. In addition, after the metallization reaction, half of the crude compound was precipitate from CH_3OH, and the rest was purified by column chromatograph (SiO_2, CH_2Cl_2/CH_3OH 200:1), then both of them crystallized from the mixture solvent CH_2Cl_2(HPLC)/n-hexane. The results of both of them match well with **1b**, displaying a porphyrin polymeric arrangement (Figure S15, right).

Regarding our experiments, and taking into account that **2a** was treated under the same conditions than **1a** and did not display coordination with H_2O, we concluded that the crystal structures, and the water content, were controlled by the conditions of the crystallization procedure. The supramolecular organization of Zn(II) porphyrin Zn(4R-PPP) and therefore the different structures found are strongly dependent on the solvent conditions.
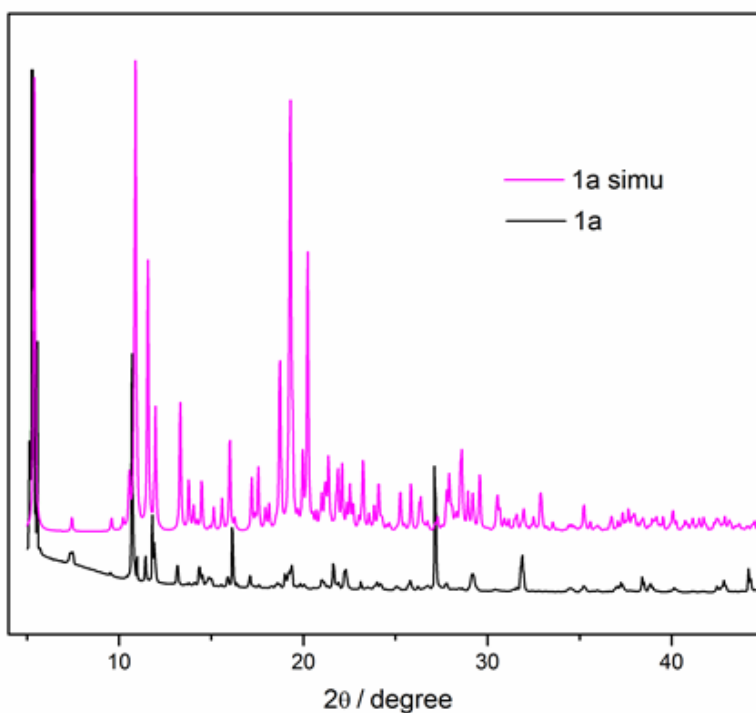
Figure S16. PXRD profiles of 1a. In black, bulk powder sample of the complex, and in pink, simulated pattern obtained from the X-ray structure.
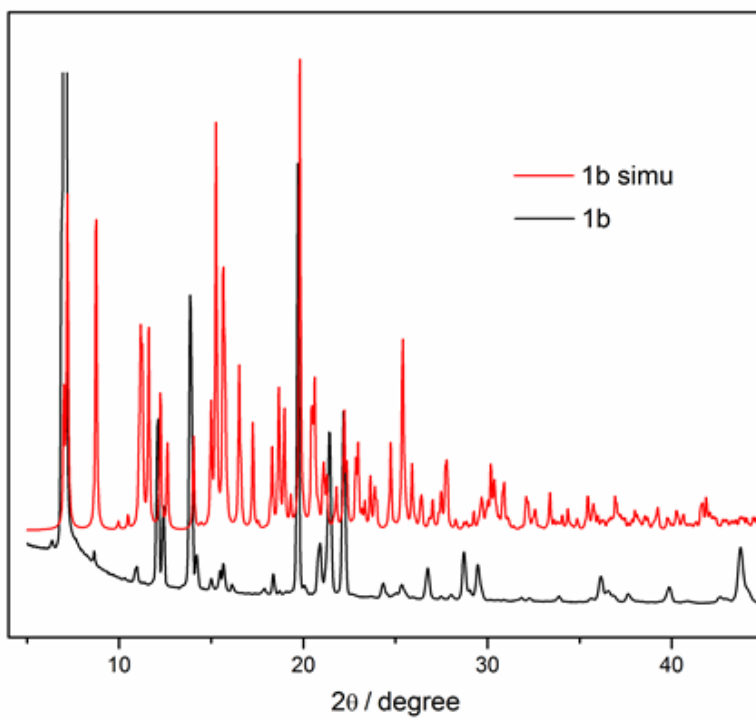
Figure S17. PXRD profiles of 1b. In black, bulk powder sample of the complex, and in red: simulated pattern obtained from the X-ray structure.
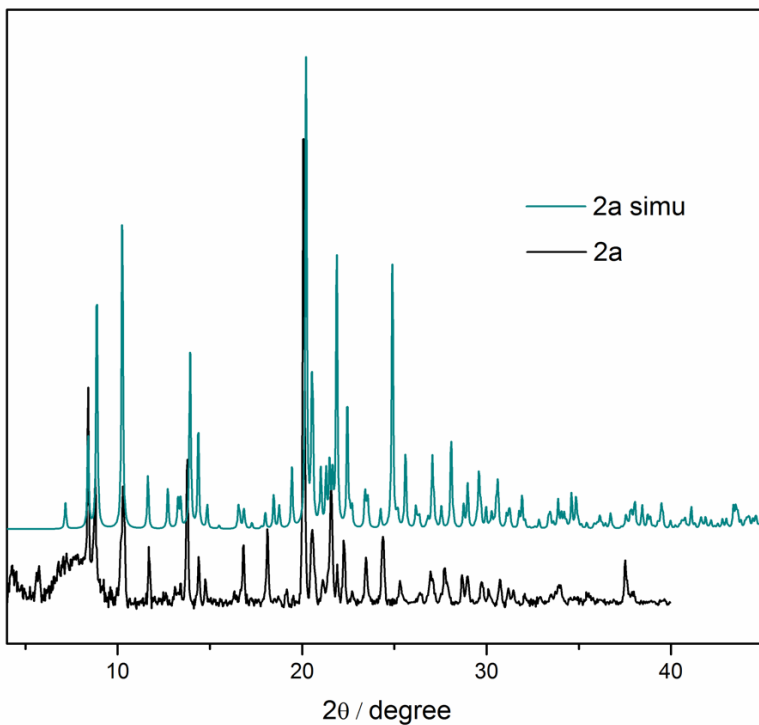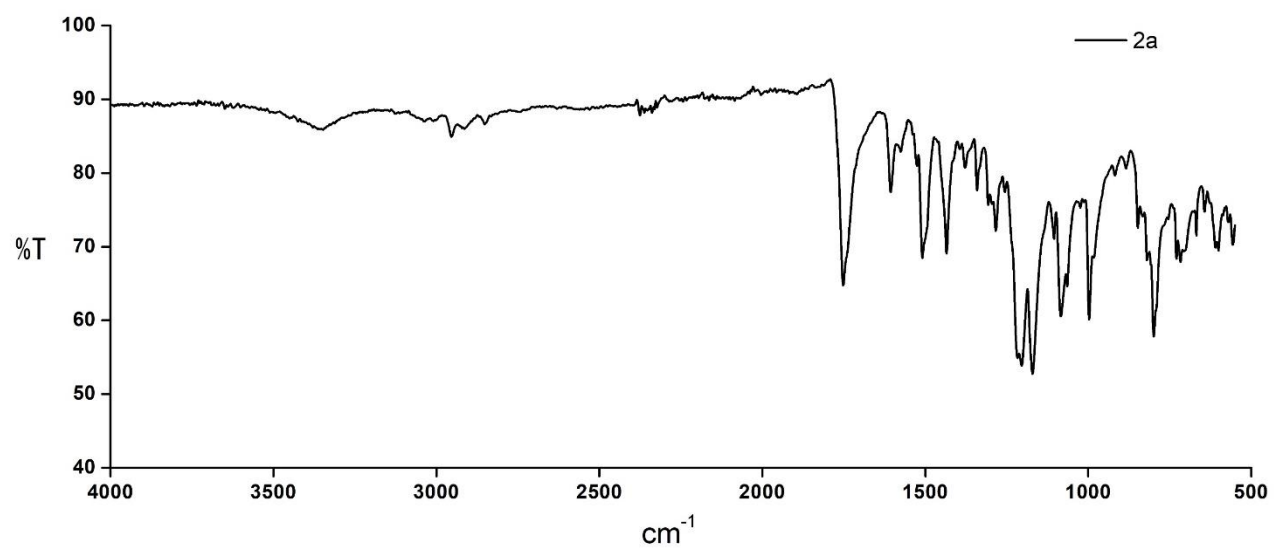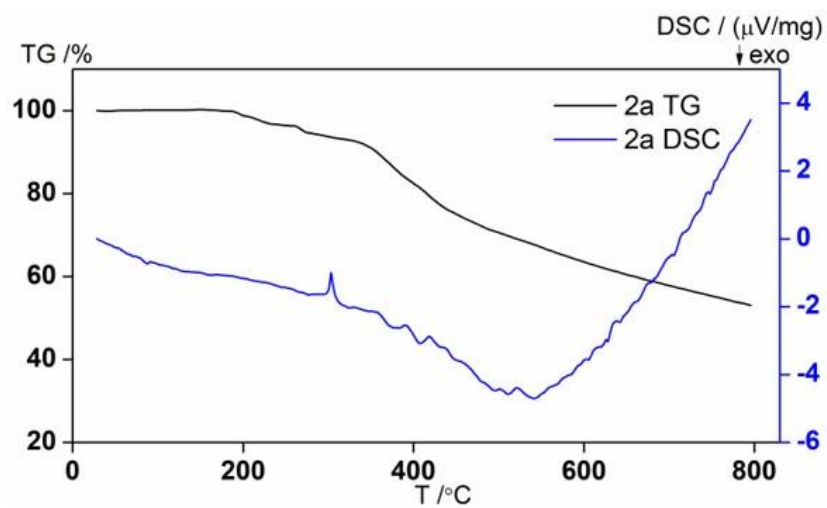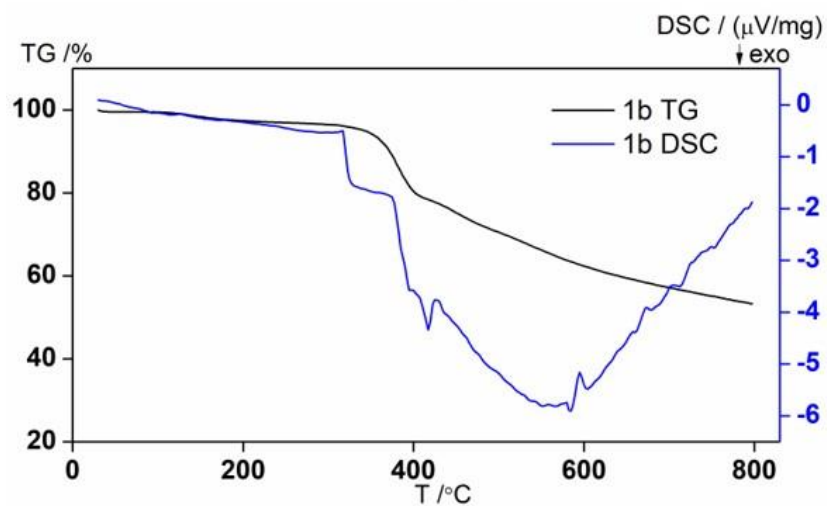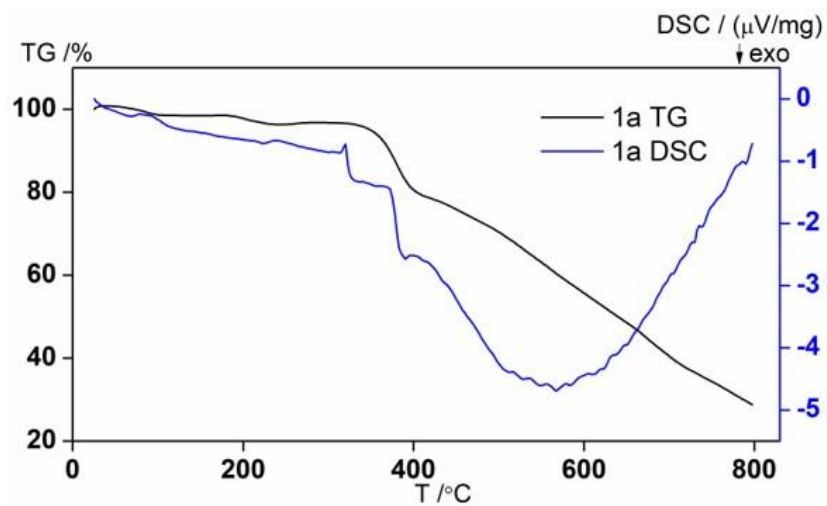
Figure S18. PXRD profiles of 2a. In black, bulk powder sample of the complex, and in green, simulated pattern obtained from the X-ray structure.
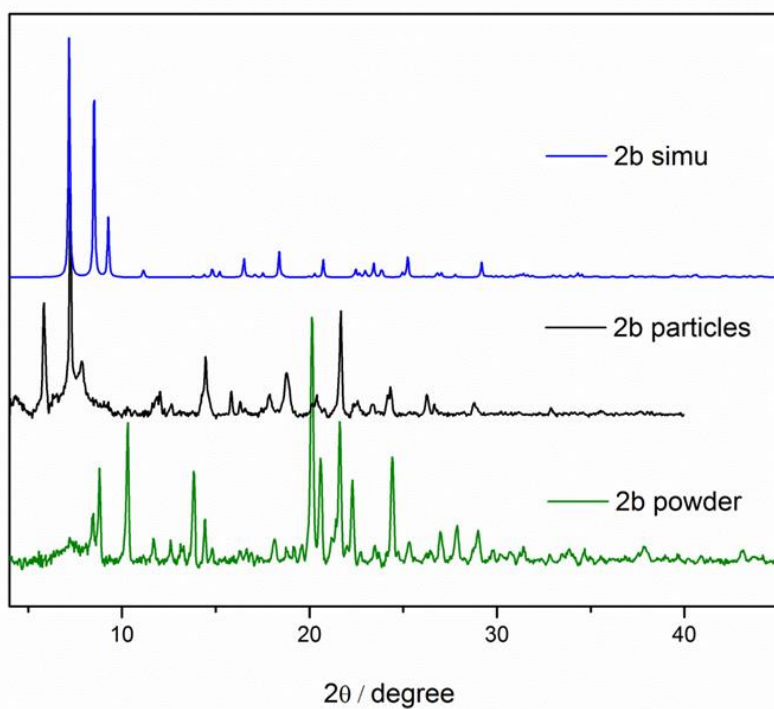
Figure S19. PXRD profiles of 2b.
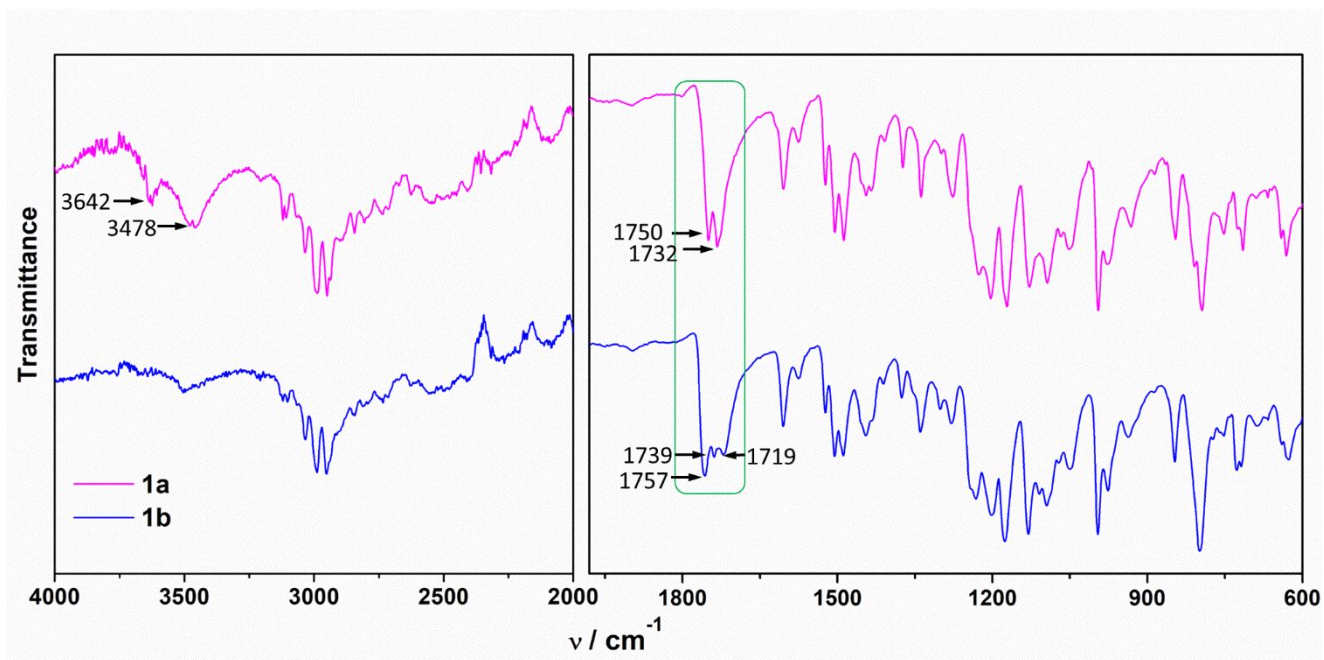
Figure S20. ATR-FTIR of **1a** and **1b**.

Figure S21. ATR-FTIR of **2a**.

Figure S22. TG-DSC graphs for **1a**, **1b** and **2a**, respectively.

Solid-state UV-Vis absorption spectroscopy.

Translucent pellets were accomplished by the mixing of 0.1 mg of each crystalline sample within 100 mg of KBr, respectively. The three spectra are almost identical, with slight shifts in their Soret bands (430 nm for 1a, 432 nm for 1b and 435 nm for 2a, respectively; detailed information in Table S6 in the SI) with an obvious higher energy shoulder in all of them, and two Q-bands, in the 558-561 nm and 599-600 nm ranges, as it occurs with the molecules in solution (Figure S14).
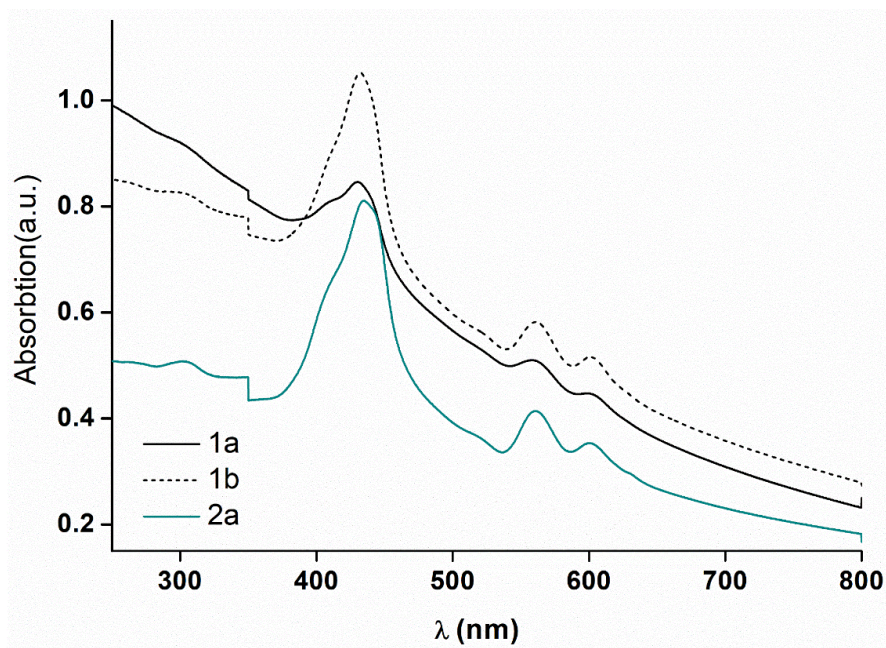

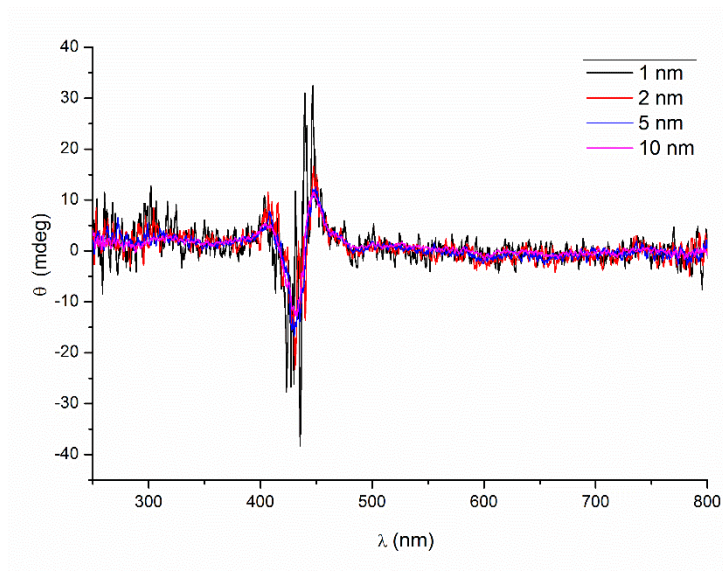**Figure S23.** The solid-state UV-Vis of **1a 1b** and **2a** crystals.
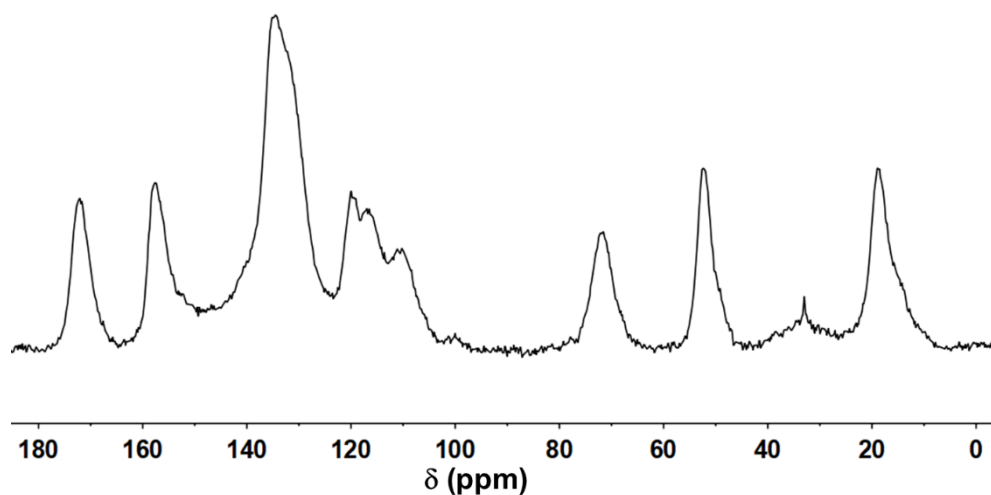
Figure S24. The solid-state ^{13}C NMR spectra of $4R$-H_2PPP between 180 – 0 ppm.
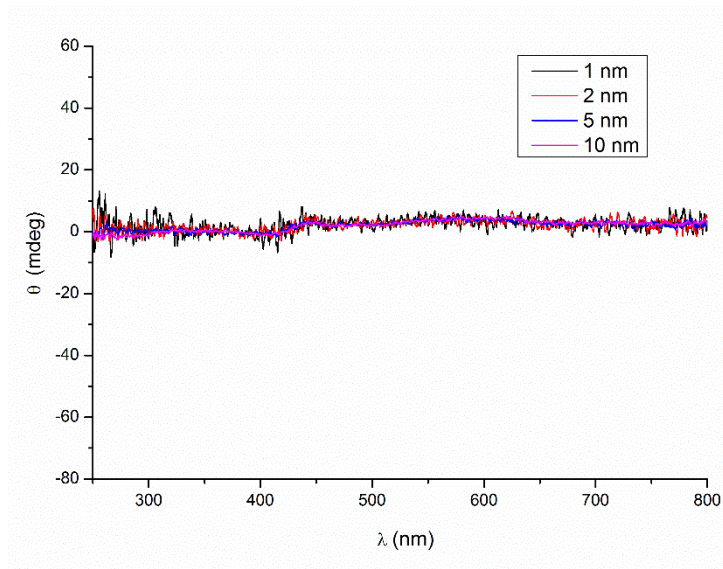
Solid-state CD spectra.

Here, both samples were grinded using an agate pestle during 5 min, 0.1 mg of the compounds (**1a-b**, **2a**) added to 100 mg of KBr and the discs were made with a pressure of 10 pa during 5 min, as thinner as possible. In addition, during the recording of the spectra the bandwidths under study were of 1, 2, 5 and 10 nm (see Figures S26-S28).
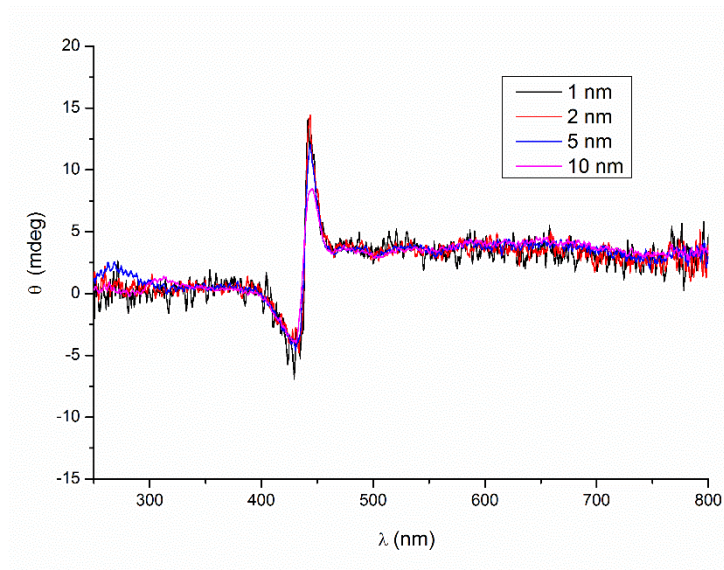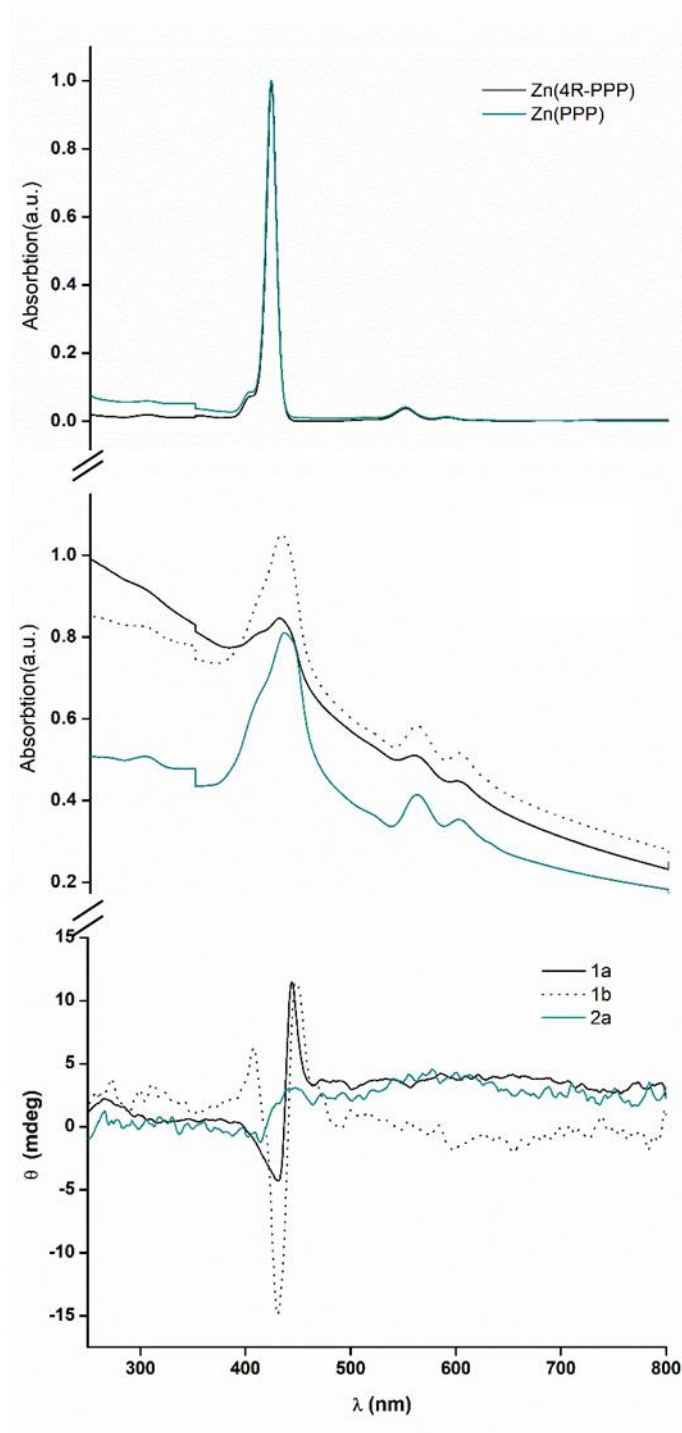

Figure S25. Solid-state CD spectra of compounds **1a**.

Figure S26. Solid-state CD spectra of compounds **1b**.

**Figure S27**. Solid-state CD spectra of compounds **2a**.

Figure S28. UV-Vis absorption spectroscopy of Zn-porphyrin in CH_2Cl_2(upper). The solid-state UV-Vis of **1a**, **1b** and **2a** crystals (middle). Solid state CD spectra of **1a**, **1b** and **2a** (lower).

Solid-state VCD studies.

Experimentally, we achieved purple pellets by mixing/milling 2 mg of the samples and 150 mg of dry KBr. An 1800 cm^{-1} cut-off filter was used with two wavelengths, 1700 and 1300 cm^{-1}, in both cases providing similar spectra. A set of spectra (five each time) were collected for 1a and 1b, respectively, where each disk was rotated at intervals of 45°.
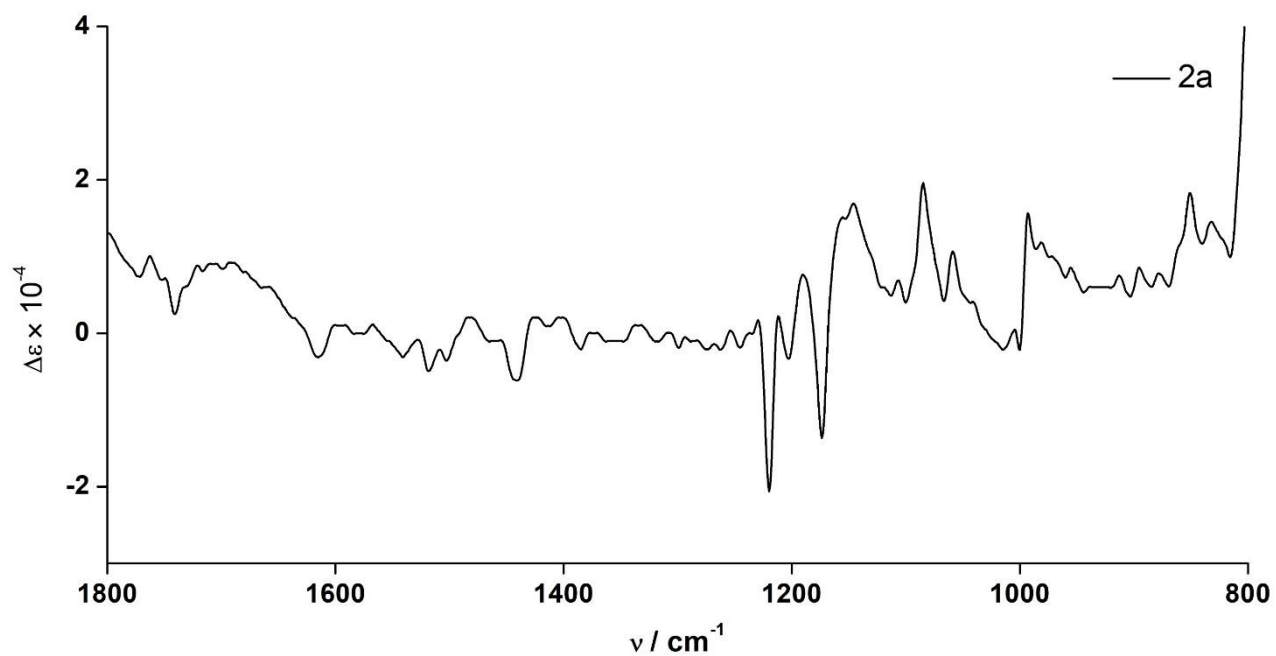
Figure S29. Solid-state VCD spectra of **2a**.
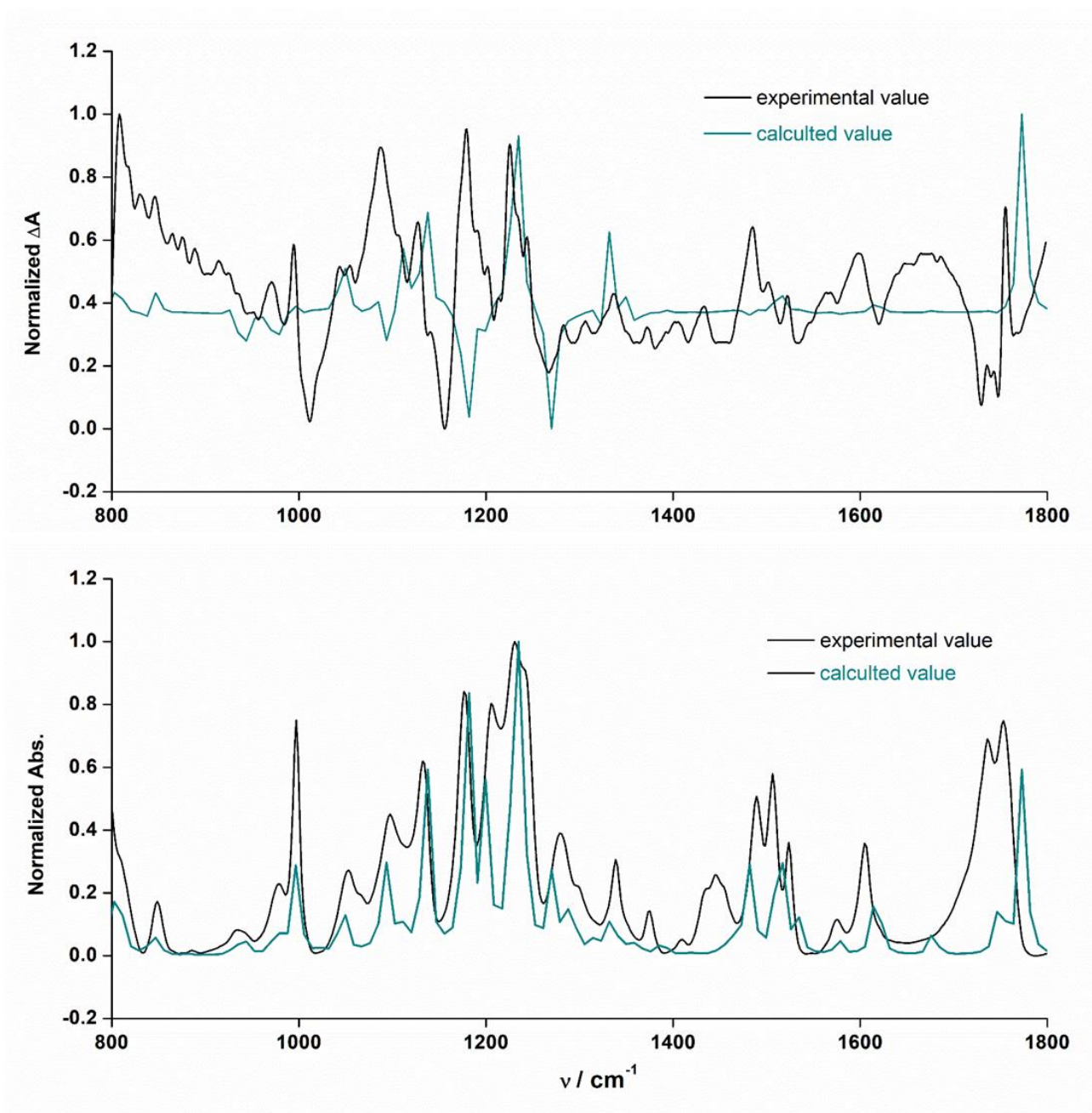
Figure S30. Theoretical calculation solid state VCD (Top) and IR (Bottom) spectra of **1a**. B3LYP calculations performed with the Gaussian09 code using a

6-311G* basis set with solvent effect included using CPCM (conductor polarizable continuum model) and a dielectric constant of 2.5 to simulate the environment of the solid. Scaling factor to the frequencies 0.98.

DFT optimized geometry   B3LYP energy   -5296.06481024 a.u.

Zn	12.72636500	4.31468200	-7.44911100
C	2.72880700	4.40663000	-8.18456400
C	2.72499100	5.85642000	-8.68395400
C	1.37420500	3.76096200	-8.46278300
C	3.13504600	7.29664800	-10.50483100
C	20.32627400	5.05701800	-5.99275800
C	19.40820400	5.89340000	-5.34889600
C	18.05036200	5.76849700	-5.60409800
C	23.91569900	4.65731000	-5.41326400
C	13.88511000	2.08916000	-5.65953900
C	15.11798800	1.65859400	-5.03578000
C	16.07678600	2.55498900	-5.38824300
C	15.44257400	3.54553500	-6.23196800
C	16.09552900	4.67147200	-6.77112600
C	15.47544700	5.69045800	-7.52079000
C	16.15688600	6.85188600	-8.05120000
C	15.22202900	7.60716100	-8.68585300
C	13.95976600	6.90890900	-8.56697600
C	12.73633000	7.36660800	-9.09561600
C	11.49729000	6.70825100	-8.96092800

C	10.25715600	7.15874800	-9.55485200
C	9.30047400	6.25443800	-9.21511300
C	9.94272800	5.23873600	-8.40890800
C	9.28895900	4.11495700	-7.86493400
C	9.90984000	3.09580700	-7.11546300
C	9.21735700	1.97198800	-6.52297500
C	10.14982100	1.22500900	-5.87398300
C	11.42258200	1.89054000	-6.04769500
C	12.64394500	1.44032200	-5.50883700
C	17.56370100	4.80774300	-6.50361700
C	18.49381900	3.98177300	-7.13762200
C	19.86385900	4.09696600	-6.89495700
C	7.81337200	3.99799500	-8.09664300
C	7.28750000	3.02366400	-8.95888800
C	5.92175700	2.91631800	-9.17805100
C	5.03398600	3.78499900	-8.53381100
C	5.53538600	4.76096600	-7.66991600
C	6.91272700	4.85680100	-7.46311700
C	12.61887300	0.18276400	-4.69398800
C	13.15738600	-1.01346900	-5.19133100
C	13.13333200	-2.18068900	-4.44149900
C	12.56882300	-2.18465900	-3.16155200
C	12.02930400	-1.00436900	-2.64640500
C	12.05938700	0.16063900	-3.41485400
C	12.09447600	-3.47998800	-1.18318700
C	10.56208900	-3.42976400	-1.18663300
C	12.57002200	-4.81679500	-0.61983400
C	8.67876700	-2.99978600	0.17815900
C	12.75093800	8.65574800	-9.85834500
C	13.35387000	8.74868700	-11.11451600
C	13.37095500	9.94400900	-11.83527000

C	12.77535300	11.08472600	-11.29341300
C	12.16722900	11.01030300	-10.03570600
C	12.15548900	9.81356000	-9.33421300
C	22.64223300	4.42408200	-6.22254600
C	22.88586300	4.78061100	-7.69364800
C	23.79974800	3.95905100	-9.71428800
C	13.36011900	12.49933200	-13.15727400
C	12.54168900	11.83644400	-14.27144400
C	13.43830100	14.00541400	-13.39450200
C	12.67082100	11.02686600	-16.49002300
H	1.19592700	3.70067900	-9.53805500
H	0.57452000	4.34305600	-8.00177600
H	2.12564100	7.70746900	-10.50104300
H	3.50102600	7.18539600	-11.52166700
H	3.79444500	7.94467600	-9.92789100
H	11.90637100	11.71382800	-16.85280100
H	19.78090700	6.63253500	-4.64848400
H	17.35193200	6.42147900	-5.09134700
H	11.58346400	-0.96775100	-1.66016000
H	12.47470300	-2.66286300	-0.56303500
H	23.74009800	4.39083600	-4.37000700
H	13.66066500	-4.84213600	-0.60904600
H	12.20505200	-4.95321700	0.39941500
H	24.20635300	5.70851000	-5.46164700
H	24.73171500	4.04490300	-5.80018800
H	15.23041700	0.79579600	-4.39732500
H	17.11348600	2.55711600	-5.08861000
H	10.13624300	8.04186400	-10.16320700
H	8.25859600	6.26782900	-9.49595700
H	8.15708300	1.78181100	-6.58827000
H	9.98912400	0.30987100	-5.32514400

H	12.62124300	2.31884000	-9.34451000
H	18.14840000	3.23423900	-7.84414400
H	20.54434800	3.43916500	-7.42145800
H	12.68290700	3.64905900	-10.13765700
H	11.68342200	9.77501600	-8.35814500
H	7.96116700	2.34396000	-9.47027400
H	5.51941400	2.16581200	-9.84944900
H	4.88103000	5.45015800	-7.15086000
H	7.28795400	5.61766600	-6.78683600
H	13.59656100	-1.02904500	-6.18343100
H	13.54497800	-3.10538100	-4.83052400
H	11.63941100	1.07141500	-3.00098800
H	2.90283400	4.44900800	-7.10536000
H	1.35801600	2.75196900	-8.04803800
H	12.20683800	-5.63835500	-1.24025100
H	8.22413000	-2.31963500	-0.54173900
H	8.51039500	-2.65166700	1.19356900
H	8.26894700	-4.00050100	0.04196000
H	17.21001600	7.06397500	-7.94898800
H	15.37273800	8.55226400	-9.18416100
H	13.81602700	7.86913900	-11.55049200
H	13.84254100	9.95883800	-12.81001700
H	11.71207100	11.90476600	-9.62513700
H	22.35129400	3.37149900	-6.15604200
H	14.36807300	12.07395000	-13.15634400
H	22.91853500	4.22070700	-10.29953200
H	24.22311000	3.01920300	-10.05796200
H	24.53480100	4.76065100	-9.78598100
H	14.03015800	14.46978100	-12.60439500
H	12.43755000	14.44158700	-13.38431600
H	13.90823800	14.21690600	-14.35631600

H	12.21205700	10.06931400	-16.24461200
H	13.45349900	10.89776400	-17.23256500
N	14.11524700	3.23440800	-6.37746500
N	14.14739500	5.75165600	-7.85565500
N	11.27567500	5.53746000	-8.28059900
N	11.24582700	3.01635800	-6.81219700
O	2.34220500	6.77791500	-8.00311900
O	3.13560700	5.96452700	-9.95018300
O	21.63965600	5.25503100	-5.65737600
O	22.65801600	5.84978600	-8.19675800
O	3.70809600	3.58849800	-8.81403900
O	12.60935900	-3.38514000	-2.50309700
O	9.85858200	-3.74822600	-2.10961800
O	10.11213500	-3.01795400	0.01074700
O	13.01465300	3.19770200	-9.35441100
O	23.43560400	3.73567600	-8.33592200
O	12.73971700	12.31540900	-11.89357600
O	11.35975700	11.61425900	-14.22720900
O	13.32878500	11.57681900	-15.32945600
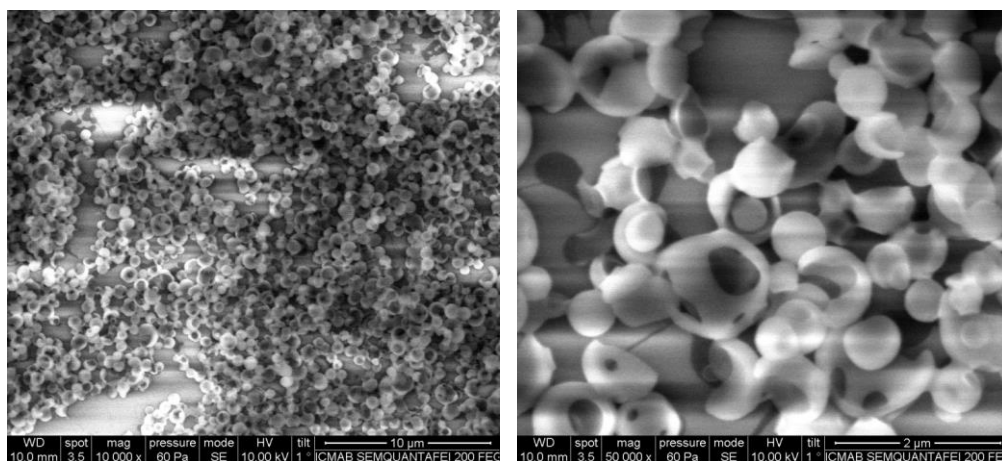
Figure S31. SEM images of Zn(4*R*-PPP) (10^{-3} M) prepared in CH$_2$Cl$_2$-CH$_3$OH (1: 1) on surface of mica
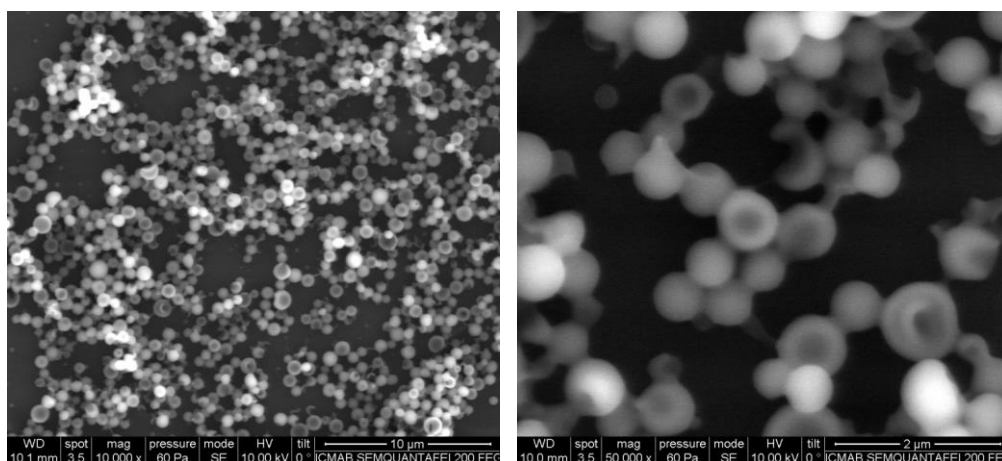
Figure S32. SEM images of Zn(4*R*-PPP) (10^{-3} M) prepared in CH$_2$Cl$_2$-CH$_3$OH (1: 1) on surface of graphite.
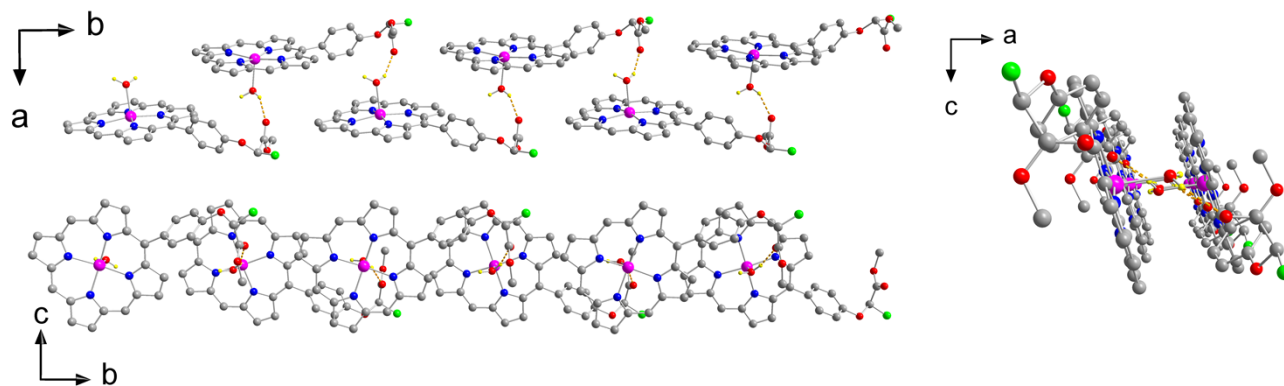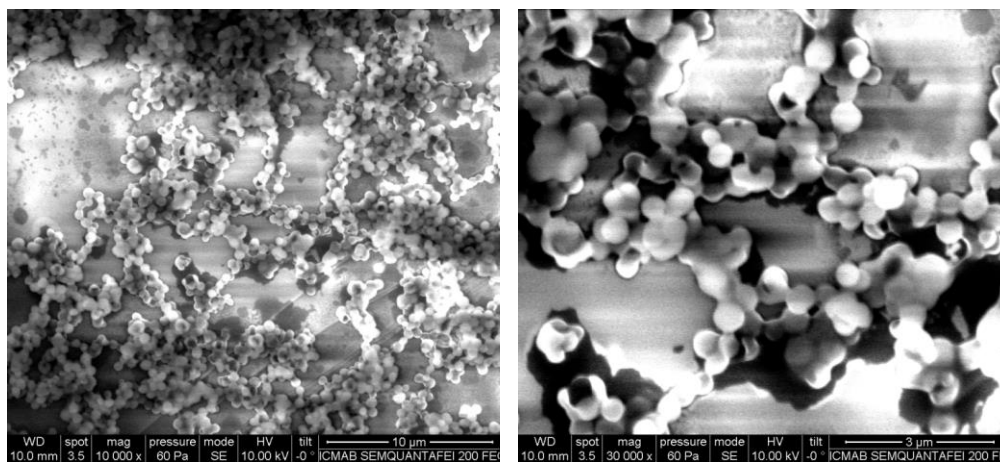
Figure S33. 1D organizations of **1a**. Colour legend: Zn in purple, O in red, N in blue, C in grey and –CH$_3$ of the coordinated branch in green
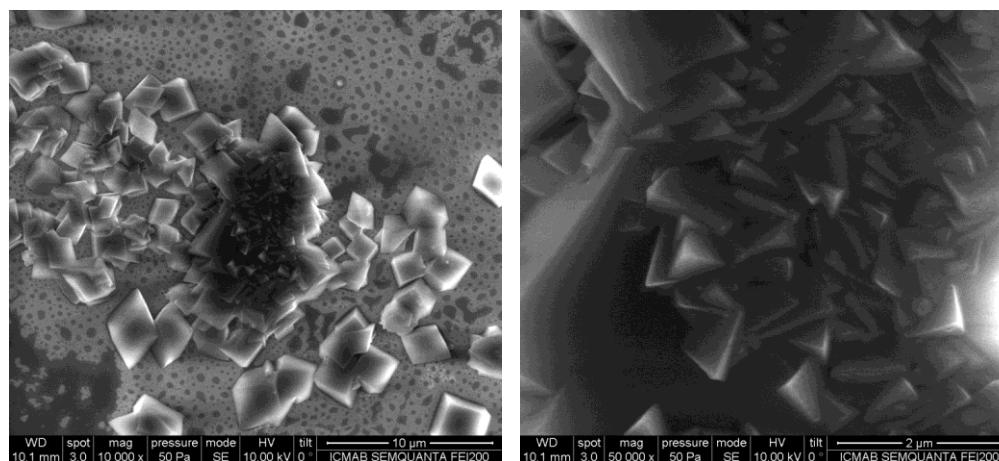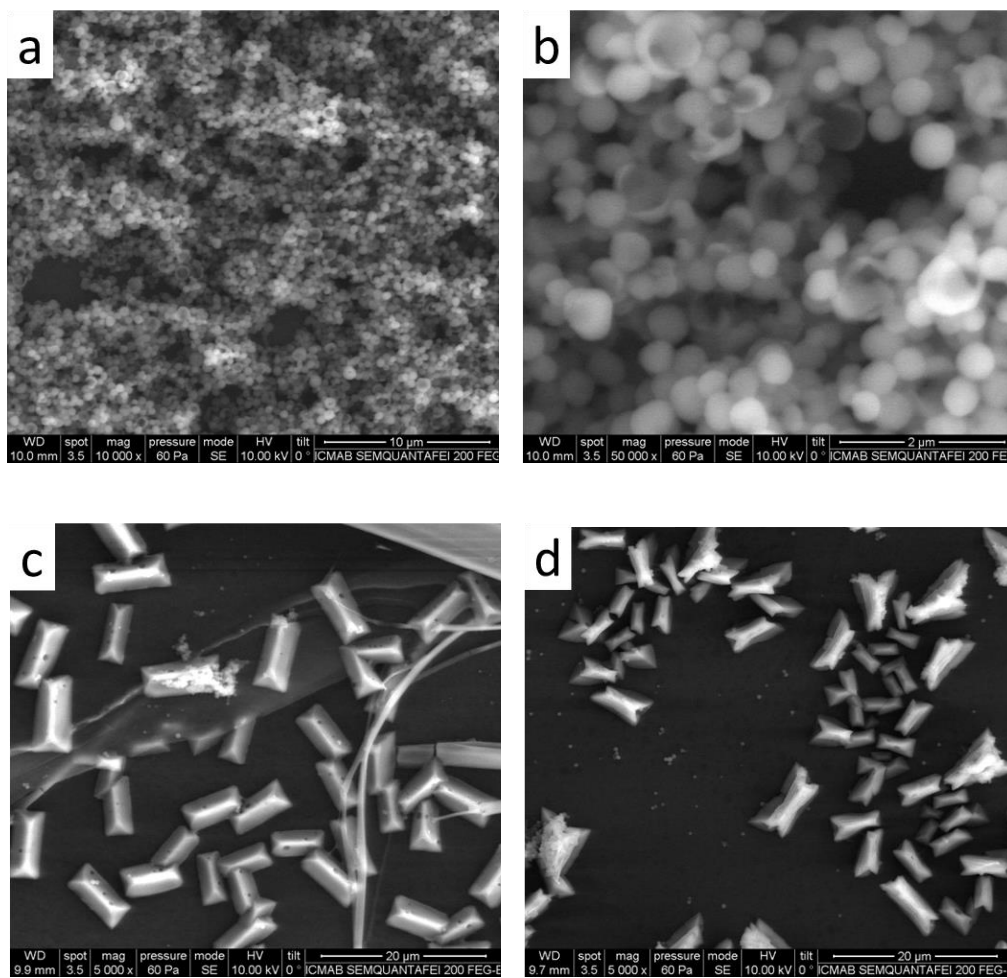

Figure S34. SEM images of Zn(PPP) (10^{-3} M) prepared in CH$_2$Cl$_2$-CH$_3$OH (1: 1) on surface of mica.
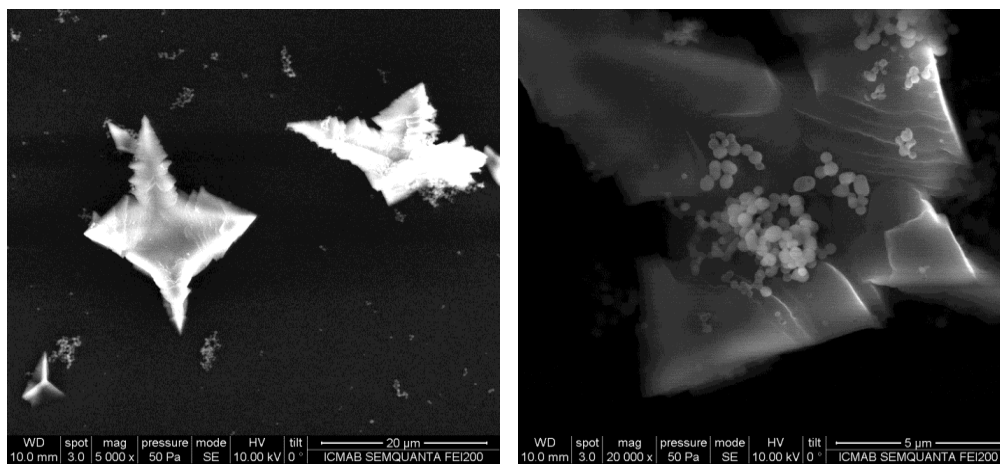
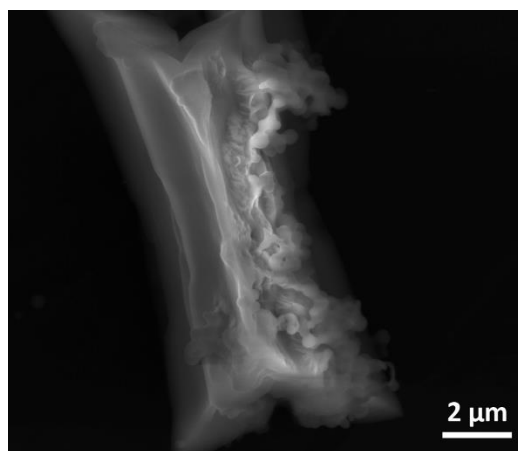**Figure S35.** SEM images of Zn(PPP) (10^{-3} M) prepared in CH_2Cl_2-CH_3OH (1: 1) on surface of graphite.

Figure S36. SEM images of Zn(4*R*-PPP) (10^{-3} M) prepared in CH_2Cl_2-hexane (1: 1) on surface of mica.
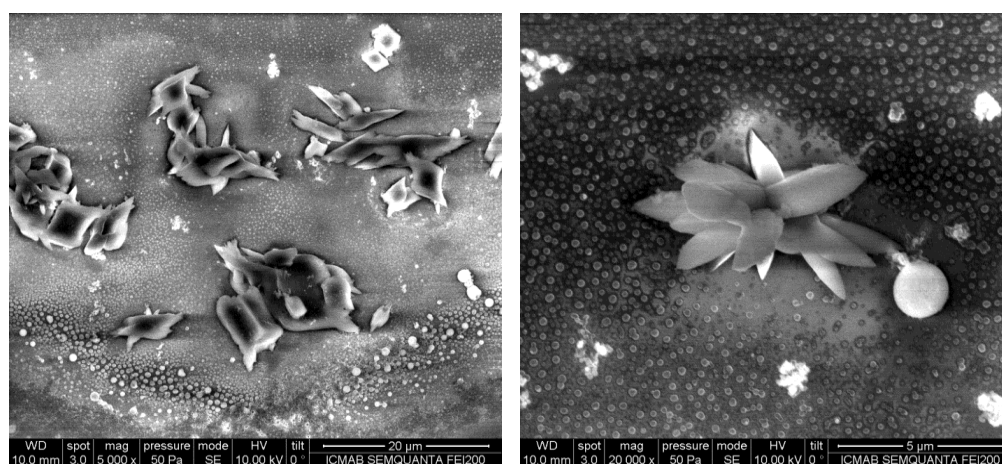
Figure S37. SEM images of Zn(4*R*-PPP) (10^{-3} M) prepared in CH_2Cl_2-hexane (1: 1) on surface of graphite in different zone (a, b) quickly evaporate of solvent, (c)in the solution drop edge, (d)in the middle of solution drop.
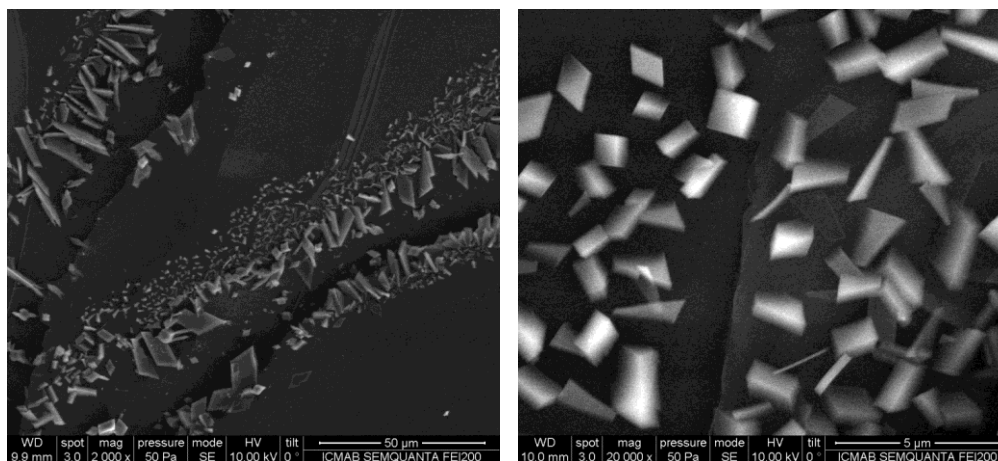
Figure S38. Zoom SEM images of Zn(4*R*-PPP) (10^{-3} M) prepared in CH_2Cl_2-hexane (1: 1) on surface of graphite.

Figure S39. SEM images of Zn(PPP) (10^{-3} M) prepared in CH_2Cl_2-hexane (1: 1) on surface of mica.

Figure S40. SEM images of Zn(PPP) (10^{-3} M) prepared in CH_2Cl_2-hexane (1: 1) on surface of (a, b) mica (c, d) graphite.

Once the aggregates formed, they were very stable and can keep their shape after 2–3 weeks delay and not disappeared. There was no difference the measurements were carried out immediately after the preparation of the thin films or many days later, even without the following metal coating normally used in SEM test.